R. & M. No. 3042
(17,929)
A.R.C. Technical Report

MINISTRY OF SUPPLY

AERONAUTICAL RESEARCH COUNCIL
REPORTS AND MEMORANDA

Experiments at $M = 1{\cdot}41$ on Elliptic Cones with Subsonic Leading Edges

By
E. W. E. ROGERS and C. J. BERRY,
of the Aerodynamics Division, N.P.L.

LONDON: HER MAJESTY'S STATIONERY OFFICE
1957
PRICE 12s. 0d. NET

Experiments at $M = 1 \cdot 41$ on Elliptic Cones with Supersonic Leading Edges

By

E. W. E. ROGERS and C. J. BERRY,
of the Aerodynamics Division, N.P.L.

Reports and Memoranda No. 3042

October, 1955

Summary.—Tests have been made at a Mach number of 1·41 on six elliptic cones forming two families of models. In the first, the vertex angle in the plane of the major axes of the elliptic cross-sections was maintained constant at 60 deg and the ratio between the minor and major axes varied; in the second family, the minor axis was constant and the vertex angle had values of 30 deg, 60 deg and 90 deg. Two cones from the first family were pressure-plotted at incidences up to 15 deg, the resulting pressure distributions being integrated to give the lift and pressure drag arising from the curved surfaces of the cones. Except for one of the pressure-plotting models, lift, drag and centre-of-pressure position were measured for all models on a strain-gauge balance. For the one cone on which a comparison was possible, good agreement was obtained for the lift and drag derived from the two methods.

The distribution of pressure on the two pressure-plotting cones was found to be approximately conical in form (*i.e.*, constant along the cone generators) and at 0 deg, good agreement with theory was obtained. At incidence, the agreement was worse and deteriorated when, at the higher incidences, transonic-type shock waves appeared on the upper surfaces of the cones. These shock waves which lay along a cone generator moved inboard with increase in incidence, and vortices, formed from flow separating from near the leading edges, also appeared, with a consequent modification of the upper-surface pressure distribution. These transonic-type shock waves were observed by using optical systems of schlieren or shadowgraph type, but with the light beam passing obliquely through the tunnel so that it was approximately parallel to the shock front; the separation vortices were detected by observing the motion of an oil film on the surface of the models.

Good agreement was obtained between linear (flat-plate) theory and experiment for the lift of the family of cones having a 60 deg vertex angle; there is only a small effect on the lift-curve slope due to increasing the cone thickness (*i.e.*, the minor axis of this family). The surface shock waves and separation vortices were responsible for a change in the rate at which the drag of the cone family increased with the lift.

The comparatively slender cone of the other family had a lift curve which was markedly non-linear at the higher incidences and this effect was attributed to the presence of separation vortices.

The inclination of the cone-like shock originating at the vertices of the models and also the distribution of pressure over the bases of the cones were measured.

1. *Introduction.*—The elliptic cone (Fig. 1) is a form which has attracted several theoretical workers in supersonic aerodynamics because of its position intermediate between the body of revolution and the triangular flat plate of zero thickness. There is little experimental information on elliptic cones however (only one other test[12] being known to the authors) and the present investigation was planned to provide additional information for comparison with theory. In addition, it was hoped that some understanding would be obtained of the flow conditions present at moderate and large incidences, when surface shock waves and boundary-layer separations become important. The latter aspect of the experiment is of particular relevance to the problems of supersonic flow over triangular and swept-back wings having subsonic leading edges, though for the elliptic cones the flow pattern is simplified by the absence of separation effects of the type found near the trailing edges of true wings.

The family of elliptic cones having the same plan-form, but different thicknesses (*see* section 2.2 below) was suitable for an investigation of the effect of thickness on the drag increment associated with the lift on the model, and hence on the amount of ' leading-edge suction ' that was present.

Published with permission of the Director, National Physical Laboratory.

Tests were made at one Mach number only (1·41) as it was considered that the cone characteristics would not differ greatly within the rather restricted Mach number range of the tunnel used.

2. *Equipment and Experimental Details.*—2.1. *The Tunnel.*—The tests were made in the National Physical Laboratory 18 in. by 14 in. High-Speed Wind Tunnel[1], the working-section of which had been calibrated previously and found to be free from serious pressure gradients. In the region occupied by the models throughout their incidence range, the Mach number in the empty tunnel varies between 1·40 and 1·42; a mean test Mach number of 1·41 was therefore used in the reduction of the experimental observations. For theoretical calculations, the value of $\sqrt{2}$ was taken as the free-stream Mach number, since this simplified the computation without introducing serious error.

During most of the experiment, the stagnation pressure of the free stream was maintained at 31 in. mercury absolute, giving a Reynolds number of $2{\cdot}0 \times 10^6$ based on the centre-line chord c of the models (Fig. 1). To determine the effect of Reynolds number changes on the model surface pressures, some tests were made at higher stagnation pressures, Reynolds numbers of 2·7, 4·0, and $4{\cdot}7 \times 10^6$ being obtained in this way.

For the measurement of the forces and moments on the cones, a three-component strain-gauge balance was used, the results obtained being reduced to lift and drag coefficients and centre-of-pressure positions. The models were supported from their bases by a slender rectangular sting (Fig. 2) which also acted as the deflecting beam in the balance system.

2.2. *The Models.*—Six cones were tested, representing two families of models. The first family had a constant value of the total vertex angle ε in the plane of the major axes of the elliptic cross-sections (Fig. 1) but different vertex angles in the plane of the minor axes. It is convenient in referring to cones of this family to denote the tangent of the half-vertex angle in the minor axis plane by $\tau/2$; τ can then be regarded as a thickness parameter for the cone, and is the ratio of the minor axis of the base ellipse to the centre-line chord of the cone (Fig. 1). This thickness ratio τ was constant for the second family of models, whilst ε varied between 30 deg and 90 deg. Thus for a stream Mach number of 1·41, the leading edge of every model was subsonic in type, though for the cone with $\varepsilon = 90$ deg, the component of free-stream Mach number normal to the leading edge was very nearly equal to unity (0·997).

Further details of the six models are given in the following Table, where μ is the ratio of the major axes of the elliptic cross-section to the minor axis.

TABLE 1

Elliptic Cone Models

(*a*) Family with $\varepsilon = 60$ deg

Model number	τ	μ	Material	Type of model
C1	0·05	23·10	Steel	For balance tests only
C2	0·10	11·55	Steel	34 pressure-plotting holes on curved surfaces
C3	0·15	7·70	Brass	For balance tests only
C4	0·20	5·77	Brass	33 pressure-plotting holes on curved surfaces

b) Family with $\tau = 0{\cdot}1$

Model number	ε (deg)	μ	Material	Type of model
C5	30	5·36	Brass	For balance tests only
C2	60	11·55	Steel	34 pressure-plotting holes on curved surfaces
C6	90	20·00	Brass	For balance tests only

The model C2 is thus common to both families.

The disposition of the pressure-plotting holes on the curved surfaces of the cones C2 and C4 was identical (apart from small inaccuracies in manufacture found in subsequent measurements and allowed for in plotting the results) and is shown diagrammatically in Fig. 3. These holes were arranged so that the distribution of pressure close to the leading edge could be determined as accurately as possible. In addition, the theoretical prediction of constant pressure along rays which pass through the vertex and along the surface at a constant fraction of the local semi-span η could be checked at $\eta = 0$ (*i.e.*, on the centre-line) and 0·4.

All models except C1 had pressure holes distributed within the base of the cone, outboard of the sting support. The readings from these holes were used to supplement the static-pressure traverses necessary to determine in detail the distribution of base pressure on the models. The bases themselves were flat, but in one case (cone C3) the base surface was subsequently modified (*see* section 6 below).

2.3. *Experimental Method and the Reduction of the Observations.*—2.3.1. *Pressure-plotting tests* (*Models* C2 *and* C4).—Incidence α was applied to the models in the plane containing the minor axes of the elliptic cross-sections (*i.e.*, in a similar manner to that for triangular wings having the same value of ε). Measurements of the surface pressures were made on the two cones at both negative and positive incidences up to the limits of the incidence gear (about plus or minus 15 deg). The agreement between the pressures at negative and positive incidences was good except at the highest values of α, where the increased blockage in the tunnel associated with a high negative incidence caused a change in the flow over the sting, an alteration of the model base pressure and a flow separation from the cone surface upstream of the base. Except in these conditions, the results at a negative and positive value of α were combined to give a distribution of pressure which was more closely defined than for a single set of readings.

The surface pressures were reduced to coefficient form C_p in the usual way. If the flow over the curved surfaces of the cone is truly conical, the normal force coefficient for those surfaces can be found from an integration of the curve of C_p against η. The pressure was not constant along the cone surfaces for small values of η, however (*see* section 3.2 below), and the integration was performed for the distribution of C_p at the middle of the centre-line chord for this range of η.

In a similar way, the chordwise force coefficient C_{XS} arising from the curved surfaces can be found by integrating the projection of the surface pressures on the cone base. The coefficient is given by:

$$C_{XS} = \tfrac{1}{2} \tan \varepsilon \int_0^{2\pi} \frac{C_p}{1 + (\mu^2 - 1) \sin^2 \theta} \, d\theta \, , \qquad (1)$$

where θ is measured from the centre of the base ellipse. The appropriate lift and pressure-drag coefficients C_{LS} and C_{DS} can be found by resolution from C_N and C_{XS}.

Because of the deflection of the pressure-plotting sting under load, a small correction has been applied to the model incidence. This correction increases with the load on the model and hence is larger, for a given incidence, at the higher Reynolds numbers.

2.3.2. *Balance tests.*—Using the balance, direct measurements were made of the normal force, total chordwise force and centre of pressure position for all cones, except C2, over a range of incidence. For the pressure-plotting cone C4 good agreement was obtained between the normal force coefficients derived independently from the balance results and from pressure integration; similarly the chordwise force measured on the balance, when corrected for the base effects described below and the contribution of the skin friction, agreed closely with the pressure-drag coefficient determined by using equation (1). Because of this agreement, no balance tests were made on the thinner pressure-plotting cone.

The highest incidence at which balance measurements could be made was dependent on either the range of the incidence gear (C5) or the strength of the sting (C1, C6) or limited by the deflection of the sting causing contact between it and the surrounding shroud. The sting deflection was also responsible for corrections to the nominal incidence. The balance itself was calibrated before and after the investigation, and at frequent intervals during the measurements.

For comparison with theory and to simplify the analysis of the experimental results, the drag coefficient required is that due to the pressure forces acting on the curved surfaces only. A correction must therefore be applied to the total chordwise force measured on the balance to allow for the pressure force of the exposed bases of the models. The distribution of pressure over the bases was found by detailed static traverses (*see* section 6 below); integration of these results gave the corresponding base pressure-force component. In a similar way the contribution of the pressure within the narrow annulus between the sting and the shroud was found. Another and less direct component arose from the pressures on the downstream end of the sting, which effectively act on the cone base over the junction of this and the sting. Finally an allowance was made for the turbulent skin-friction force over the curved surfaces of the cones, and this was assumed to contribute 0·0030 to the total chordwise force coefficient.

After corrections have been applied for these effects, the residual coefficient is directly comparable with C_{xs} found using equation (1).

All balance tests were made with a fixed transition position near the leading edge*.

2.3.3. *Flow observations.*—The pressure-plotting and balance tests were supplemented by schlieren and shadowgraph photographs of the flow around the model; surface-film studies were also made to show the boundary-layer transition and separation.

3. *Pressure, Distribution and Surface-Flow Results.*—3.1. *Spanwise Pressure Distributions at Zero Incidence* (*Cones* C2 *and* C4).—Simple conical flow theory suggests that for the elliptic cone models the distribution of pressure in the spanwise direction is similar at all chordwise positions if the distribution is plotted in terms of a fraction of the local semi-span η. Since the present terms were made at zero yaw, only one half of the span need be considered, the experimental points from both sides being superimposed.

In considering the pressure distribution at zero incidence, it is convenient to expand the region near the leading edge of the cone by plotting C_p against a parameter ξ, equal to $\cos^{-1}\eta$. The results for the two pressure-plotting cones are shown in Figs. 4a and 4b.

The scatter of the experimental points in the neighbourhood of the leading edge cannot be considered as excessive having regard to the very open scale of η in this region. On the centre-line and at $\eta = 0{\cdot}4$, there is a progressive decrease in C_p towards the bases of the models, indicating that the flow is not truly conical. This effect persists at incidence and is discussed further in section 3.2 below.

* Without transition bands on the model, there were, at low incidences, occasional changes in the chordwise force measured on the balance, which were attributed to alterations in the extent of the laminar flow reaching the trailing edge. All balance tests were therefore made with transition occurring near the leading edge. It is considered (*see* section 3.5.2) that in these tests the flow pattern at high incidence is not greatly affected by the actual boundary-layer state near the leading edge.

The experimental results can be compared with several theoretical predictions of the pressure distribution, all of which assume a conical type of flow. The earliest theory was developed by Squire[2], who in 1947 used a special set of co-ordinates to obtain a solution of the linearised supersonic-flow equation. He showed that to the first approximation the pressure was constant across the span. It was realised by Squire at that time that the solution must fail near the leading edge, and in 1951, Hurley[3] improved upon Squire's solution by inserting a pair of line sources, each passing through one set of the foci of the elliptic cross-sections. The necessary surface conditions were satisfied at the cone centre-line, and at the leading edge. The resulting surface shape is nearly that of an ellipse, being somewhat sharper very close to the leading edge.

An alternative approach is to regard the elliptic cone as a more general case of a circular cone. Thus Ward's slender-body theory[4] can be extended, as Fraenkel[5] has done, to slender bodies of elliptic cross-section. The spanwise pressure distribution for elliptic cones is then obtainable in a particularly simple form. A similar method, giving identical results[6] is due to Kahane and Solarski[7].

The more complex second-order theory has been worked out by Van Dyke[8]. In its simplest form this adds to the slender-body equation for the spanwise pressure distribution a single second-order term, yielding what Adams and Sears[36] have called the ' not-so-slender-body ' theory; a more complete analysis, includes further second-order terms*.

If the flow field near the body apex is known, the pressure distribution on slender bodies without axial symmetry can be obtained by using Ferri's linearised characteristics method[9]. A development of this method[10] can be applied to elliptic cones, the linearised flow solution for these shapes being superimposed upon the known, non-linear solution for a circular cone. This technique (which has the advantage of dealing with the effects of cone incidence) is most suitable for elliptic cones of a roundish cross-section rather than the wing-like cones of the present investigation. For this reason, and the fact that the method of Ref. 10 is not simple in application, no comparison has been made between the experimental results and this theoretical solution in the present paper.

Another method too complex for simple comparison with the experimental data was developed by Maslen[11] in 1948. The required elliptic boundary is obtained by a suitable internal distribution of sources and sinks, but for an elongated ellipse, the requisite number of sources and sinks is large and the method becomes tedious. A comparison of Maslen's method with some experimental pressure distributions obtained on an elliptic cone† at $M = 1{\cdot}89$ is given in Ref. 12.

In contrast with all these theories is one due to Van Dyke[13]. This corrects the results of thin-wing theory near round leading edges at which the normal component of the free-stream Mach number is subsonic, and is thus directly applicable to the elliptic cones. A correction, which varies with spanwise position, to Squire's original results can be found quite simply by this method.

The comparison between theory and experiment of the spanwise pressure distribution at zero incidence for cones C2 and C4 is given in Figs. 4a and 4b. The slender-body theory predicts pressures which are everywhere too low on both cones and far better agreement is obtained by using the not-so-slender-body theory. Van Dyke's second-order theory (omitting triple products) represents a further stage of refinement, but for the thinner cone, the agreement with experiment is less good than for the not-so-slender-body theory.

The theory developed by Hurley is most satisfactory when applied to the thinner cone, but even for the other pressure-plotting model‡, the discrepancy between this theory and experiment is not large. The irregular shape of the theoretical curve close to the leading edge would seem to be inherent in the type of approach used by Hurley.

---

* When this report was written, only the second-order solution, omitting the triple products, was available for comparison with experiment. The inclusion of these terms improves the agreement between theory and experiment somewhat (*see* Ref. 8).

† For this cone, $\varepsilon = 37$ deg, $\tau = 0{\cdot}21$ and $\mu = 3$.

‡ Ref. 3 does not contain the solution for an elliptic cone with $\tau = 0{\cdot}2$; the results used in Fig. 4b were calculated by Mr. W. E. A. Acum.

Van Dyke's edge-correction method is a simple modification of Squire's linearised solution, the magnitude of the correction becoming greater as the leading edge is approached; considering the approximate nature of the method the theoretical curve is remarkably close to the experimental points.

It is interesting to note that the differences between these various theoretical solutions are relatively small and for the thicker cone at least are comparable with the experimental scatter. In general the agreement between theory and experiment is good.

3.2. *Spanwise Pressure Distributions at Incidence (Cones* C2 *and* C4).—As was explained in 2.3.1. above, well-defined spanwise pressure-distribution curves can be obtained by combining the results for the negative and positive values of a given incidence. These curves are presented in Figs. 5a and 5b.

For comparison with theory it is more convenient to consider the increment of pressure coefficient $\Delta C_{p\alpha}$ caused by the incidence. This increment is well known[14] for a triangular flat plate and this can be regarded as the solution appropriate to an infinitely thin elliptic cone ($\tau = 0$). Alternatively, Taylor[15] has considered the cross-flow about a slender elliptic cone and has derived an expression for the spanwise distribution of $\Delta C_{p\alpha}$ which includes the effect of changing values of τ, for a given plan-form.

The experimental pressure-coefficient increments for typical incidences of 2·0 deg, 5·1 deg, and 10·2 deg are shown in Figs. 6a to 6c, together with some theoretical curves. At the lowest incidence, the flat-plate solution agrees well with the experimental distribution except close to the leading edge, where the finite-edge radius of the cones becomes important. Taylor's solution, whilst giving finite values of $\Delta C_{p\alpha}$ in this region over-estimates their magnitude; for the remainder of the semi-span, the predicted pressure increment is also too large. This should be expected, however, since the Taylor theory gives a lift-curve slope equal to the slender-body or small aspect-ratio value, which is considerably higher than that predicted by flat-plate theory. The ratio between these two slopes is a factor $1/E$, where E is a complete elliptic integral of the second kind, dependant[14] on ε and M; for $\varepsilon = 60$ deg and $M = 1{\cdot}41$, $E = 1{\cdot}26$. If the results given by Taylor's theory are divided by E, thus giving very nearly the experimental lift*, the modified curve of $\Delta C_{p\alpha}$ for cone C4 at $\alpha = 5{\cdot}1$ deg is in closer agreement with experiment over most of the surface than the flat-plate theory (Fig. 6b). At the highest incidence shown (10·2 deg), the experimental results indicate that the low-pressure region has begun to spread inboard from the leading edge, and a pronounced pressure recovery takes place at about $\eta = 0{\cdot}7$. As is shown below, this represents a departure from the conditions assumed by potential theory and as a result neither of the theories can describe satisfactorily the upper-surface pressure-distribution. On the lower surface, where the increase in incidence has occasioned no unexpected change in the flow pattern, the modified theory of Taylor's agrees remarkably well for both cones.

The decrease in surface pressure, from vertex to base, along the lines represented by $\eta = 0$ and $\eta = 0{\cdot}4$, already noted at zero incidence, exists at incidence also; the effect is shown graphically in Figs. 7a and 7b. Though the precise value of the mean pressure gradient is uncertain due to the experimental scatter, it would appear to be largely independent of incidence for both cones, and for the thinner cone, to be similar in magnitude for both values of η. With the other pressure-plotting cone, the pressure gradient decreases away from the centre-line and at this position is about double the corresponding value for the thinner cone. Because of this pressure-gradient effect, the curves shown in Figs. 5a and 5b have been drawn for conditions at one-half of the centre-line chord.

It is perhaps necessary to point out that there is no pressure gradient in the empty tunnel in this region, and it seems likely that the effect is real, particularly as its magnitude increases with model thickness.

Owing to the intense spanwise pressure gradient near the leading edge, the existence of similar pressure changes along lines of constant η cannot easily be investigated. What evidence there is

* There would seem to be little theoretical justification for this procedure.

(for example from the holes at $\eta = 0{\cdot}985$) suggests that the effect, if it exists, is smaller than the experimental scatter.

If the pressure coefficient on the centre-line at $0{\cdot}58c$ is plotted against incidence (as in Fig. 8), the variation is seen to be dissimilar for the two surfaces. The lower surface curve is similar in shape to that for a family of circular cones of semi-vertex angle equal to that between the elliptic cone surface at $\eta = 0$ and the free-stream direction at each incidence. On the upper surface up to about 7 deg incidence there is a similarity between the experimental decrease in pressure with incidence and that predicted theoretically for a flat-plate wing of the same planform.

3.3. *Surface Shock Waves.*—For small values of incidence, the pressure minimum on the upper surface progressively decreases; the rate at which the decrease occurs is reduced at the higher incidences until finally, the pressure near the leading edge becomes insensitive to further changes in incidence (Fig. 9), which produce instead an inward spread of the low-pressure region (Figs. 5a and 5b). The marked similarity between the development of the spanwise pressure distribution with incidence for the elliptic cones, and the change with incidence of the chordwise pressure distribution on a two-dimensional aerofoil at subsonic speeds[16], suggests that the rapid pressure recovery obtained inboard of the leading edges at high incidences on the cones may be due to a transonic-type shock wave positioned at a constant value of η, and lying normal to the cone surface.

The existence of surface shock waves has been demonstrated conclusively by Love and Grigsby[17], using an elegant optical technique. If the swept leading edge is regarded as part of an infinite swept wing, then the shock waves may be considered as arising from the subsonic component of the free-stream velocity normal to the leading edge. The cross-section of the cone normal to the leading edge is an ellipse, and hence it might be expected that shock waves would appear on the cone surface soon after critical conditions are reached for a two-dimensional elliptic cylinder of the appropriate thickness $0{\cdot}745\tau$ and incidence 2α in a stream of Mach number $0{\cdot}705$. The critical value of α may be calculated using Ref. 18, but is much lower than that found experimentally for both the pressure-plotting cases (C2 and C4.) This suggests that a two-dimensional analogy of this kind is unsatisfactory, and it is probably more realistic to regard the surface shock waves as disturbances originating from the cone apex and propagating along the cone surface at approximately the Mach angle of the local surface Mach number. The shock waves turn the flow (which is inclined a little towards the cone centre-line as a result of the acceleration in the leading-edge region) back in the direction of the main-stream flow, a process which is continued isentropically to the rear of the surface shock waves.

Since the flow field around the cones is nearly conical, the surface shock waves should lie near the leading edge at a constant value of η, and hence will not be visible in schlieren photographs of the conventional type where the light beam passes through the tunnel normal to the stream direction. They can be seen however if the light beam is made to pass through the tunnel at angle ϕ to the stream direction so that it is approximately along the shock front (Fig. 10). Oblique-beam photographs of schlieren and shadowgraph type were obtained for a range of incidence on both pressure-plotting cones; small surface shock waves were first observed at incidences of $7{\cdot}1$ deg and $4{\cdot}1$ deg for cones C4 and C2 respectively.

With increase in incidence, the shock waves grow and move inboard, as shown in Figs. 11a and 11b, and the flow later separates from the model surface. At the higher incidences multiple shocks appear in the photographs. These arise from the fact that the shock waves lying in the somewhat irregular flow above the separated layer are probably curved and no longer follow a line of constant η (*see* Ref. 39 for an analogous condition on a two-dimensional aerofoil). In addition, for the constant beam inclination ϕ used in Fig. 11 the apparent separation increases as the shock front moves inboard*. The light beam also traverses part of the model wake and this

* The curved shock waves become visible as apparently discrete waves when the light beam is nearly tangential to the local shock front.

obscures some of the details of the flow; in addition, some definition is lost due to scattering from the glass side walls of the tunnel. By taking photographs at slightly different values of ϕ, and making certain assumptions, an approximate estimate of the mean spanwise position of the shock waves can be made, though the accuracy is not very great at the highest incidences.

One check on the shock position is possible, however, at an incidence of 10·0 deg. For this incidence, schlieren photographs were taken with the model mounted upon a cranked sting and rotated through 90 deg, so that its plan-form was normal to the light beam. The surface shock waves show up as thin lines in the wake behind the model and intersect the base at $\eta = 0{\cdot}88$ and $\eta = 0{\cdot}79$ for the cones C2 and C4. Corresponding values for the shock position deduced from the oblique-beam photographs were 0·89 and 0·82, indicating reasonable agreement.

In Fig. 12, the spanwise shock position is plotted against incidence, together with a diagrammatic representation of the changes in the spanwise pressure distribution. At low incidences, just after the formation of the shock wave, the peak suction occurs just outboard of the shock wave (as for a two-dimensional aerofoil). For the thinner cone (C2) the shock remains approximately at the rear end of the constant-pressure region at the higher incidences, the main rapid recompression occurring well inboard of the shock front. The shock wave is similarly outboard of the rapid compression region for the other cone.

The inaccuracies in determining the location of the shock wave are insufficient to account for the discrepancy between the shock position and the main recompression, and it seems probable that the surface shock waves are not directly responsible for the pressure increase.

3.4. *Separation Vortices.*—The existence of vortices lying just above the upper surface of delta wings at incidence is now well-known at low speeds[19–22]. These vortices are fed by the flow separating near the swept leading edge of the wing and are generally situated at an approximately constant value of η. Örnberg[22] has shown that they also exist at supersonic-flow velocities and that there is a marked similarity between the surface flow in such cases and that obtained at low speeds. The theoretical effect of the separation vortices on the wing characteristics has been discussed by Brown and Michael[23], Adams[24] and Küchemann[38].

Vortices, formed in a similar manner from the separating cross-flow, also occur with bodies of revolution when these are at incidence in subsonic and supersonic streams[25, 26]. Since the elliptic cone is a form intermediate between the delta wing and the body of revolution, separation vortices are likely to occur on the present models.

To detect their presence, a technique similar to that developed by Örnberg was used. A mixture of thick oil, titanium oxide and oleic acid* was rolled onto the model surface to form an even film, which then flowed under the action of the air forces. The mixture tended to accumulate and move slowly rearward in regions of separated flow and to be removed rapidly from places where the local velocity is high. On the two cones tested in this way (C2 and C4), the oil accumulated at the higher incidences in a band situated at a constant value of η some distance inboard of the leading edge, which is fed from the immediate leading-edge region as a result of the pressure gradient there, and on its inboard edge by oil transferred outwards by the rotation of the separation vortex lying above the surface. The oil accumulation thus represents a region of separated flow, the directions of the separating flow being opposed at the inboard and outboard edges of the band. The former edge was always well-defined, but the latter tended to be rather diffuse.

The scoured region inboard of the accumulated oil is a trace of the separation vortex lying somewhere above it. Within the region, the cone surface was covered with fine sinuous lines of oil, inclined in the centre of the trace at about 45 deg to the free-stream direction; these are presumably the streamlines of the surface flow. The actual position of the vortex in relation to its surface trace is not known, but if a criterion often employed for low-speed tests is used (namely,

* The titanium oxide, being white, assists in illustrating the motion of the surface fluid; the oleic acids act as a decoagulant and is only used in small quantities.

that the vortex is immediately above the point of inflection of the surface streamlines as indicated by the oil), then the vortex would seem to be directly above the centre of the trace.

From shadow photographs similar to those shown in Fig. 11b, flow separation appears to occur near the leading edge at incidences of about 7 deg and 10 deg for the two pressure-plotting cones. These values are in approximate agreement with the lowest incidences at which an accumulation of oil, and inboard of this a scoured region, were observed (6·1 deg and 10·2 deg for cones C2 and C4 respectively), though the boundaries of the trace itself were very diffuse. It is doubtful in fact whether a true vortex had formed from the separating flow in these cases. These incidences also correspond approximately to the beginning of the inboard spread of the low-pressure region (Figs. 5a and 5b) and the limitation of the peak suction achieved on the upper surface (Fig. 9).

As the incidence is increased, the vortex trace decreases in width and becomes more marked, whilst the region of accumulated oil is more clearly defined at the inboard edge. The stopping process of the tunnel often tended to obscure the surface pattern and hence photographs of the vortex traces were taken whilst the tunnel was running. Typical examples of these are shown in Fig. 13. From such photographs and visual observations the approximate width of the trace was found and this is plotted, together with the extent of the separation region in Fig. 12. The vortex trace (and hence presumably the vortex) lies just inboard of the rapid recompression zone observed in the spanwise pressure distribution, which must arise from the action of the pair of symmetrically-disposed vortices in accelerating the air between them towards the cone surface, thus creating a quasi-stagnation effect. A similar distribution of pressure in the region of the separation vortices has been noted in tests on bodies of revolution at supersonic speeds and on triangular wings at low speeds. In the latter case, a local suction peak is induced on the wing surface immediately underneath the vortex, which usually lie therefore outboard of the pressure recovery region, and not inboard, as seems to be the case for the present tests.

Like the surface shock waves, the separation vortices persist in the model wake and hence showed up as faint diffuse bands in the schlieren photographs taken at $\alpha = 10$ deg with the models rotated so that the plan-form was normal to the light beam.

The flow pattern in the cross-flow plane (to which must be added the velocity component along lines of constant η if the true flow is to be obtained) may be similar to that sketched in Fig. 14, but more work is required to confirm this. Örnberg[22], for example, has suggested for low-stream speeds, a more complex pattern involving a pair of subsidiary vortices.

The effect of changes in leading-edge sweep on the surface oil pattern at a fixed incidence of 10 deg was investigated on the rotated models mentioned above, the incidence gear now being used to apply yaws of up to 15 deg. Some photographs of the resulting flow patterns are shown in Fig. 15. If the two leading edges can be regarded as independent, then the well-marked trace and separation region for a 75 deg swept leading edge (15 deg yaw) corresponds to the flow over cone C5 (where $\varepsilon = 30$ deg) at 10 deg incidence. The opposite edge is swept at 45 deg and thus is representive of cone C6. In this case the separation region has moved inboard, the flow remaining attached to the surface back to about $\eta = 0{\cdot}85$. A surface shock wave may exist at this position and may be responsible for inducing the flow separation.

The results shown in Fig. 15 suggest that as the leading-edge sweep increases, the incidence at which separation vortices appear decreases. This effect has been noted before in low-speed tests[22].

3.5. *Boundary-Layer Transition and Reynolds-Number Effects.*—3.5.1. *Zero Incidence.*—At zero incidence and without transition bands, sublimation tests using hexachlorethane[40] as an indicator, showed that transition to fully turbulent flow occurred on cones C2 and C4 some distance behind the leading edge. As can be seen in Fig. 16, numerous wedges of turbulent flow originating from the leading-edge region were usually present and the position of the transition front was extremely sensitive to both surface conditions on the models and the air-flow in the tunnel.

For the thinner cone (C2) only, the region between the fully developed turbulent flow and a position just inboard of the leading edge was filled with traces of boundary-layer vortices, arising from the three-dimensional instability of the laminar flow around the swept leading edge. These traces, shown in Fig. 16, were parallel to the stream and spaced approximately uniformly along the leading edge at about 70 to the inch. It is apparent that the critical conditions for causing this type of boundary instability at the Mach and Reynolds numbers of the present tests lie somewhere between those provided by the two pressure-plotting cones*. Unfortunately no sublimation tests were made on the cone having an intermediate value of the thickness parameter.

3.5.2. *At incidence.*—At small incidences the transition pattern is little different from that observed at $\alpha = 0$ deg. Above about 3 deg incidence, the transition front moved forward progressively with increase in cone incidence. On the upper surface this is probably due to the unfavourable pressure gradient present inboard of the suction peak (*see* Fig. 5), whilst on the lower surface the three-dimensional instability of the laminar boundary layer is aggravated by incidence[27]. At higher incidences, when surface shock waves are present on the upper surface, the transition front seems to be at the shock position but the nearness of this to the leading edge before flow separation occurs makes the sublimation pattern difficult to interpret. This problem is even more acute when the flow finally leaves the model surface not far from the leading edge.

A transition band placed near the leading edge of pressure-plotting cones would unfortunately interfere with the numerous pressure holes in that region and hence the pressure distributions were measured with the transition taking place at its natural position. A few check measurements were made (with a restricted number of holes) for some incidences on both cones with a leading-edge transition band in position. No significant change in the surface pressures was found, however. It was concluded from this that the state of the boundary-layer immediately upstream of the flow separation or shock-wave system did not seriously affect the overall flow pattern and the forces on the model.

This view was strengthened by the good agreement obtained between the lift and drag deduced from balance readings and pressure distributions on cone C4 (*see* section 4 below) and from tests made at an incidence of $10{\cdot}2$ deg at Reynolds numbers greater than those of the bulk of the tests. Because the turbulence in the tunnel tends to increase with tunnel total pressure (and hence test Reynolds number for a given model), it is probable that the pressure distributions shown in Figs. 17a and 17b were obtained with a turbulent boundary layer starting at the leading edge. The results shown in Fig. 17 are somewhat complicated by the increased sting deflection as the tunnel total pressure is increased, but in general change in the shape of the pressure distribution is small. There would seem to be an increase with Reynolds number in the magnitude of the pressure rise caused by the separation vortex (an effect noted elsewhere), but the position of the rise is not altered appreciably.

4. *Force and Centre-of-Pressure Measurements.*—4.1. *Lift.*—The lift curve for cone C4 derived from integrating the surface pressure distribution was in good agreement with that determined from strain-gauge-balance measurements (Fig. 18a), thus indicating the reliability of the two methods.

For the family of cones with vortex angles of 60 deg, the lift curves are approximately linear (Fig. 19a). There is a small thickness effect on the slope of the curves, that of the thinnest cone ($\tau = 0{\cdot}05$) being in almost exact agreement with linearised flat-plate theory. For comparison, the small aspect-ratio (or slender-body) curve is included in this Figure.

A similar set of curves for the cone family with constant thickness ($\tau = 0{\cdot}10$) is presented in Fig. 19b. Cone C6 ($\varepsilon = 90$ deg) has a leading edge which is almost sonic at the Mach number of the present tests, and, as in other experiments on triangular wings with similar leading-edge conditions, the lift-curve slope is rather less than that predicted by theory.

* Ref. 27 includes an equation suitable for determining the critical conditions on a swept wing at low speeds; this is not suitable for applying to elliptic cones.

The curve for the cone having a 30 deg vertex angle, unlike the others, is markedly non-linear. Up to about 7 deg incidence, the experimental results agree closely with the flat-plate theory (but not the small aspect-ratio theory which is some 7 per cent greater in slope), but thereafter the lift increases with incidence at a greater rate. This non-linearity is due to the separation vortices shed from the upper surface, a similar effect having been noted for bodies of revolution[25]. A simple cross-flow approximation to allow for the non-linear lift characteristics of small aspect-ratio wings has been given by Flax and Lawrence[28], who suggest the following equation:

$$C_{LS} = \left(\frac{\partial C_L}{\partial \alpha}\right)_{\text{linear theory}} \alpha + C_{Dc}\,\alpha^2, \quad \ldots \quad \ldots \quad \ldots \quad \ldots \quad (2)$$

where C_{Dc} is the drag coefficient of a two-dimensional cylinder of the appropriate cross-section when this is placed normal to an oncoming stream at a Mach number M sin α. For an approximate value of C_{Dc} for elliptic cylinders, the low-speed* drag coefficients given by Delany and Sorenson[29] may be used; C_{Dc} is about 1·7 for cone C5. The substitution of this value in equation (2) leads to a non-linear effect somewhat larger than that found experimentally.

Legendre[20] has given an approximate theoretical treatment for the effect of separation vortices on the lift of slender delta wings having sharp leading edges. This theory was improved by Adams[24], who also calculated the lift by a different method based on the work of Munk[30]. Both theories predict an increase in lift above the small aspect-ratio value proportional to $\alpha^{5/3}$, the coefficient of this term being different in the two cases. More recently, Küchemann[38] has evolved a lifting-surface theory for wings with sharp leading edges which gives a non-linear term proportional to $\alpha^{2/3}$.

The leading edge of the cone C5 is not sharp and hence the theoretical predictions of Adams and Küchemann would not be expected to be in agreement with experiment (Fig. 19c). For round leading edges, Küchemann suggests that the value of α in the non-linear term should be measured not from zero-lift conditions but from the onset of flow separation and the formation of vortices. The drag results suggest that some flow separation (perhaps only locally) takes place at a very small incidence. The lift curve, on the other hand, departs from linear theory at about 5 deg incidence. If the latter value is used as an indication of the formation of separation vortices and used in the way suggested by Küchemann, a curve in reasonable agreement with experiment is obtained.

It is perhaps of interest to note that the experimental points differ from linear theory at the higher incidences by an amount which is proportional to about $\alpha^{1\cdot9}$. If the non-linear contribution is considered to be proportional to incidences measured above 5 deg, then the non-linear term varies like $(\alpha - 5)^{2\cdot5}$.

The accuracy of the theoretical prediction of the non-linear lift curve must depend, in the end, on the closeness of the mathematical flow model to that actually present on the wing (this point is discussed in Refs. 23, 24 and 38). On these grounds, Küchemann's method of approach would seem to be preferable.

The lift results for all six cones are given in Table 2.

4.2. *Drag.*—In Fig. 18b, a comparison is made between the pressure drag of the curved surfaces of the cone C4, as found by integrating the experimental pressure distribution, or deduced from the balance readings. The agreement between the two sets of points is remarkably good in view of the difficulties inherent in both methods.

The zero-lift values of C_{DS} for the two cone families are plotted in Figs. 20a and 20b. For the cones having a 60 deg vertex angle, C_{DSO} is proportional to τ^2 and some 25 per cent greater than that predicted by slender-body theory[5]. This difference would be expected, as the theoretical

* For $\alpha = 15$ deg, $M = 1\cdot41$, the value of the cross-flow Mach number (M sin α) is 0·365, which is sufficiently small to justify the use of low-speed data.

values of C_p for the cone surface are smaller than those found experimentally (Figs. 4a and 4b). For the family 4b with constant-thickness parameter, C_{DS0} is rather unexpectedly proportional to ε.

These zero-lift drag coefficients can be expressed as a fraction of the theoretical drag[31] of a semi-infinite circular cone having the same base area (Fig. 21). This ratio is less than unity for all the cones tested but it approaches this value as ε decreases.

At incidence, it is convenient to consider the increment in the pressure-drag coefficient (ΔC_{DS}) from the zero-lift condition. This increment will therefore be the streamwise component of the additional resultant force coefficient caused by the application of incidence. If this force acts normal to the stream direction, the drag due to lift will be zero; if it acts normal to the chordline, the increment is then $C_N \sin \alpha$, or $C_{LS} \tan \alpha$. Curves of ΔC_{DS} against $C_{LS} \tan \alpha$ are plotted in Figs. 22a and 22b, for the two cone families. Also shown are the curves for the condition where the resultant force due to lift is normal to the chord (*i.e.*, no ' leading-edge suction '), and the drag increment obtained when the full ' leading-edge suction ' predicted by linear theory[14] for a flat-plate triangular wing is developed.

For the cone family having a constant value of τ, the experimental curves lie close together at small incidences with a slope approximately equal to that obtained with the full theoretical suction. At higher incidences, there is a change in slope, the curves now becoming nearly parallel to the ' no leading-edge suction ' line.

By plotting these results on a larger scale it is possible to represent the curve for each cone satisfactorily by two straight lines, as shown diagrammatically in the upper half of Fig. 23. The incidence at which these lines intersect (α_k) when plotted against thickness as in Fig. 23, is in agreement with the values of incidence at which shock waves were first observed on the upper surfaces of the cones. The drag curves can be analysed more carefully for the two pressure-plotting cones by considering the variation with $C_{LS} \tan \alpha$ of the contribution to ΔC_{XS} of each surface alone, where ΔC_{XS} is the change in chordwise force coefficient from that observed at zero lift. The results for cone C4 are shown in Fig. 24.

Both surfaces are now seen to have curves to which a simple two-line representation is a reasonable approximation, α_k being about $6 \cdot 0$ deg and $7 \cdot 6$ deg for the lower and upper surfaces respectively (the mean value found from the drag-increment curve was $7 \cdot 3$ deg). The change in slope of the upper-surface curve would seem to be caused by a slowing down of the rate at which the peak suction increasing with α (*see* Fig. 9), which first takes place when the surface shock waves form (about 7 deg incidence). With the loss of the appropriate low pressure near the leading edge, the chordwise force on the surface decreases at a less rapid rate, till by 10 deg, the peak surface suction has been limited and the only decrease in chordwise force can come from the inboard spread of the low-pressure region. Low pressures at stations inboard from the leading edge are less effective however in reducing ΔC_{XS} as the incidence is increased, because of the consequent increase of θ in equation (1) on page 3. Briefly then, the transition region in the slope of ΔC_{XS} curve for the upper surface corresponds to a change in the spanwise pressure distribution from the low-incidence type (having a peak suction near the leading edge) to the high-incidence type (with a large constant-pressure region spreading inboard from the leading edge).

The failure of the upper-surface flow to maintain the rate of decrease of chordwise force for that surface is offset to a considerable extent by a similar (though opposite) change in slope of the lower-surface curve shown in Fig. 24, caused in this case by an inboard spread of a high-pressure region, originally limited to the leading-edge region, with incidence. As is shown in Fig. 6c, the development of the lower-surface pressure distribution with incidence is closely in accordance with the predictions of a modified slender-body theory and it therefore seems reasonable to suppose that the shape of the lower-surface curve shown in Fig. 24 is independent of the non-potential flow phenomena which occur at higher incidences on the upper surfaces*.

* This implies that either the drag due to lift is reduced at the higher incidences because of the lower-surface pressure changes, or that there is a compensating change on the (potential) upper-surface pressure distribution to maintain a constant slope in the ΔC_{DS} vs. $C_{LS} \tan \alpha$ curve.

The sum of the chordwise force increment contributions from the two surfaces is the change in C_{XS} from its zero-lift value. This is also shown in Fig. 24. At the higher incidences, ΔC_{XS} reduces very slowly, indicating that its capacity to modify the $C_N \sin \alpha$ term in the drag equation is small.

In the other cone family, the model having a vertex angle of 90 deg has a curve with a slope appreciably lower than 45 deg (Fig. 22b), despite the fact that with an almost-sonic leading edge, there should be little theoretical reduction due to leading-edge suctions. Moreover, surface shock waves should be present at all incidences with a consequent increase in drag.

The slender cone (C5) should, however, benefit from its highly swept leading edges in the rate at which its drag increases with lift. The experimental results suggest that the theoretical reduction in drag is not attained even at very small incidences, the drag-coefficient increment being almost exactly equal to $C_{LS} \tan \alpha$. This may be due to local flow separations present near the leading edges at low incidences, which limit the peak suctions attained on the upper surface. As the incidence is further increased, these separation bubbles develop into separation vortices with a resultant non-linear lift curve.

For a slender body at small incidence, the drag-coefficient increment caused by the lift is approximately $\frac{1}{2}C_L\alpha$, or half the 'no leading-edge suction' value[4]. The difference between this line and that obtained experimentally for cone C5 illustrates the magnitude of the drag increase caused by the separation phenomena.

The drag results for the six models are tabulated.

4.3. *Centre-of-Pressure Position.*—Together with C_{LS} and C_{DS}, the centre-of-pressure positions for the models are tabulated in Table 2, where they are given as a fraction f of the cone centre-line chord downstream from the theoretical position[14] at two-thirds of this chord. For all cones tested on the balance, f is less than $0{\cdot}01$, which suggests that the theoretical assumption of conical flow is obtained in the experiment. There is a small thickness effect for the family with $\varepsilon = 60$ deg, the centre-of-pressure tending to move forwards with increase in thickness (Fig. 25a), but this change is of the same order as the possible experimental error, and should be regarded with some caution.

5. *The Inclination of the Cone-Vertex Shock.*—The inclination σ between the free-stream direction and the cone-like disturbance originating from the model vortex can easily be found in the plane containing the minor axes of the elliptic cross-sections σ' from schlieren photographs taken with the light beam normal to that plane. Results for the two families are shown in Fig. 26; for clarity the experimental points have been omitted.

On the upper surface, σ' reaches a minimum for all cones except C6 at about the incidence at which the cone surface on the centre-line becomes parallel to the stream. The curve for the lower surface has a similar shape for most cones, with a point of inflection at a moderate incidence. Only with cone C5 ($\varepsilon = 30$ deg) is the curve different in shape, the values of σ' varying only slowly with α.

In Fig. 27a, the shock inclination at zero incidence is plotted against τ and ε. In the plane of the minor axes, the measured values agree well with those predicted theoretically for circular cones of the same base area. The value of σ in the plane of the major axes of the elliptic cross-sections can be estimated approximately from schlieren photographs by means of the nearly hyperbolic intersection of the disturbance with the tunnel window (this method is only strictly applicable when the disturbance in the plane is truly conical, but the error is probably not large within the incidence range of the present tests).

The value of σ in the minor-axes plane is smaller than that in the major-axes plane when the models are at zero incidence, though this difference is small except for the cone with $\varepsilon = 90$ deg. As a result, the shock profiles around the models are almost circular in shape.

In the case of the 90 deg cone, the leading edge is almost sonic and the shock is probably highly curved close to the leading edge[35].

The shock inclination in the major-axes plane could be measured directly only in the tests made on the cranked sting at 10-deg incidence. The variation of σ around the model at this incidence is probably similar to that shown in Fig. 27b. There is some distortion from the truly circular form and from the zero incidence profile.

6. *Base Pressures.*—As was mentioned in section 2.3.2, the distribution of pressure over the bases of all cones except C2 was determined to allow for the contribution of this region to the total chordwise force measured by the balance. The transition bands near the leading edges of the model, used during the balance tests to ensure a forward transition position, particularly at low incidences, were retained during the measurement of the base pressures.

The variation of base pressure in a direction parallel to the minor axis of the base ellipse was small for all the models tested and was therefore neglected. The spanwise distribution for cone C4 at different incidences is shown in Fig. 28a. The supporting sting and balance shroud extend to about $\eta = 0{\cdot}2$ for this particular model, but their influence seems to be felt well outboard of this position. The broken curves represent the mean of the pressures on the exposed base above and below the shroud. The actual difference in pressure was small, except at the highest incidences.

There is a characteristic minimum in the ratio of the base pressure to the free-stream static pressure λ which occurs at about $\eta = 0{\cdot}8$, and which is more pronounced at incidence. A similar minimum was observed by Chapman, Wimbrow and Kester[32] near the tip of a rectangular wing of single-wedge section at $\eta = 1{\cdot}50$*, and has also been reported in other N.A.C.A. tests.

The measurements made on cone C4 and shown in Fig. 28a only just extend into the incidence range in which separation vortex traces were observed ($\alpha > 10$ deg). The extent of the rapid recompression region on the curved surfaces of the cone (*see* Fig. 5b) is denoted by the line A in Fig. 28a, and the width of the vortex trace by B. Together the zones A and B occupy the region of increasing base pressure. It was noticed that in the few cases where a comparison of this type could be made, the spanwise position of the vortex trace was near the outboard end of the region of approximately constant base pressure.

The base-pressure distribution curves at zero incidence for the five cones are plotted in Fig. 28b. From this, the mean base pressure (with respect to η) can be found for the region between $\eta = 0{\cdot}3$ and $0{\cdot}9$ (*i.e.*, neglecting the effects of the support, and the extreme tip, where the curve is not defined clearly). These mean values of λ are plotted in Fig. 28c in terms of the ratio of the minor axis of the base ellipse to the major axis $1/\mu$. For the cone family of constant plan-form, the points fall on a curve which can be regarded as of a satisfactory form to connect the appropriate base-pressure ratios of a two-dimensional model and a body of revolution[32–34]. The results for the other cone family show a smaller decrease in the mean value of λ as the base ellipse approaches a circle. This is consistent with the arguments of Ref. 33, which imply that for a given value of μ, an increase in vertex angle should give a mean base pressure which is nearer the two-dimensional value.

The results so far discussed were obtained on models whose bases were flat. The effect of a cavity in the base of cone C3 is shown in Fig. 28d. This cavity was about the local base thickness in depth around the sting junction, but decreased in depth towards the tips of the model. It had a considerable effect in reducing the variation of base pressure both with spanwise position and incidence, presumably by increasing the volume of the dead-air region. The complete drag of the cone (*i.e.*, including the base drag) was increased by about 4 per cent at zero incidence but was

* Ref. 32 associated this local region of low pressure with the shedding of tip vortices from the wing even at zero lift. No such vortices were detected in the present tests, however, though some aperiodic eddies causing a lower mean pressure near the tip might be present. Alternatively the low-pressure region may be associated with the reduction in the effective Reynolds number of the flow over the base as the tip is approached (*see* Ref. 33).

reduced at $\alpha = 3{\cdot}6$ deg. A cavity base might prove useful in other tests similar to those described in the present report, by reducing the extent of the traverses required to determine the base pressure distribution.

7. *Concluding Remarks.*—In this experiment an analysis of the forces experienced by the model in terms of the pressure distribution over the curved surfaces of the cone was restricted to two models of 60 deg vertex angle. The accuracy with which the surface pressure distribution can be predicted at zero incidence is reassuring. At incidence, the position is not so satisfactory. Because of its elegance and comparative simplicity, an extension of Van Dyke edge-correction method[13] to the incidence case would be valuable.

When surface shock waves and separation vortices are present, there is an appreciable modification of the spanwise pressure distribution, with the vortices causing steep pressure increases. Existing theories deal mainly with the effect of the shed vortices on the characteristics of a model having sharp leading edge and predict a non-linear lift curve. This was only observed with the smallest cone (C5) and a simple cross-flow representation or a modification of the theory of Ref. 38 give theoretical lift curves in moderate agreement with that found experimentally. For the cone family having a 60 deg vertex angle the lift curves are linear over the incidence range of the experiment, and depart little from that predicted by flat-plate theory, even for the thickest cone of this family.

One interesting effect of the upper-surface flow phenomena on this cone family is the alteration in the rate at which the drag changes with lift. Surface shock waves and flow separation near the leading edge cause a transition from a state where the full theoretical leading-edge suction is attained to one where the chordwise force remains almost constant as the incidence is increased, the consequent drag rise being due almost entirely to the $C_N \sin \alpha$ component. A similar progression of events probably occurs for true delta wings. The present tests indicate the importance of leading-edge radius in determining the range of low-drag flow.

The true delta wing will exhibit a more complex flow pattern than was found for the elliptic cones and more complete understanding of the relative importance of the separation vortices and surface shock waves must be obtained before the aerodynamic characteritics of such wings can be predicted with any confidence.

8. *Acknowledgements.*—Many members of the N.P.L. High-Speed Group assisted in the tests described in this report. Particular acknowledgement is due, however, to Mr. N. C. Lambourne, who was responsible for the design and use of the strain-gauge balance, and who pointed out the simple method of obtaining C_{DS} from pressure integrations, and the possible advantages of the cavity base. Mr. P. Peggs and Miss B. M. Davis gave particular assistance in both the experimental work and in the major task of analysing the results.

Finally, the authors wish to acknowledge the interest shown by Dr. Milton Van Dyke of the N.A.C.A. in the pressure distributions obtained at zero incidence and his help in making the comparisons between theory and experiment shown in Figs. 4a and 4b.

LIST OF SYMBOLS

c		Chord of cone on centre-line
f		Centre-of-pressure position rearward of $2/3c$
C_{Dc}		Drag coefficient of elliptic cylinder with major axis normal to stream
C_{DS}		Pressure-drag coefficient of curved surface of cone
C_{DS0}		Pressure-drag coefficient of curved surface of cone at zero incidence
ΔC_{DS}	$=$	$C_{DS} - C_{DSO}$
C_{LS}		Lift coefficient of curved surface of cone
C_N		Normal-force coefficient
C_p		Pressure coefficient
$\Delta C_{p\alpha}$		Increase in C_p above zero-lift value
C_{XS}		Chordwise force coefficient of curved surface of cone
ΔC_{XS}		Increase in C_{XS} above zero-lift value
E		Complete elliptic integral of the second kind (*see* Ref. 14)
M		Mach number
R		Reynolds number, based on centre-line chord
α		Cone incidence, with respect to free-stream direction
α_k		Incidence at which change in drag due to lift is assumed to occur
ε		Total vertex angle of cone, in plane of major axes of elliptic cross-sections
η		Ratio of spanwise position to local semi-span
θ		Angle, measured around base ellipse from major axis (*see* Fig. 1)
λ		Ratio of local base pressure to free-stream static pressure
μ		Ratio of major axis of elliptic cross section
ξ	$=$	$\cos^{-1}\eta$
σ		Inclination of vertex shock to free-stream direction (σ' in plane of minor axes of elliptic cross-sections)
τ		Ratio of minor axis of base ellipse to centre-line chord
ϕ		Inclination of light beam to free-stream direction in oblique optical systems
ψ		Angle in plane normal to stream direction measured from cone vertex (*see* Fig. 27b)

REFERENCES

No.	Author	Title, etc.
1	D. W. Holder	The 18 in. × 14 in. High-Speed Wind Tunnel of the N.P.L. (In preparation).
2	H. B. Squire	An example in wing theory at supersonic speeds. R. & M. 2549. February, 1947.
3	D. G. Hurley	The pressure on the surface of a flat elliptic cone set symmetrically in a supersonic stream. C.P. 109. November, 1951.
4	G. N. Ward	Supersonic flow past slender, pointed bodies. *Quart. J. Mech. App. Math.* Vol II. No. 1., p. 79. 1949.
5	L. E. Fraenkel	Supersonic flow past slender bodies of elliptic cross-section. R. & M. 2954. May, 1952.
6	C. H. E. Warren	Supersonic flow about slender bodies of elliptic cross-section. *J. Ae. Sci.* Vol. 21, p. 57. 1954.
7	A. Kahane and A. Solarski ..	Supersonic flow about slender bodies of elliptic cross-section. *J. Ae. Sci.* Vol. 20, p. 513. 1953.
8	M. Van Dyke	The slender elliptic cone as a model for non-linear supersonic-flow theory. *J. Fluid Mech.* Vol. I, p. 1. 1956.
9	A. Ferri	The linearised characteristics method and its application to practical non-linear supersonic problems. N.A.C.A. T.N.2236. 1950.
10	A. Ferri, N. Ness and T. T. Kaplita	Supersonic flow over conical bodies without axial symmetry. *J. Ae. Sci.* Vol. 20, p. 563. 1953.
11	S. H. Maslen	Method of calculation of pressure distributions on thin conical bodies of arbitrary cross-section in supersonic stream. N.A.C.A. T.N.1659. 1948.
12	S. H. Maslen	Pressure distributions on thin conical body of elliptic cross-section at Mach number 1·89. N.A.C.A. R.M. E8K05. (TIB 2061). 1949.
13	M. D. Van Dyke	Subsonic edges in thin-wing and slender-body theory. N.A.C.A. T.N.3343. 1954.
14	A. Ferri	*Elements of Aerodynamics of Supersonic Flows.* Chapter 15. The Macmillan Company. 1949.
15	C. R. Taylor	The pressure distribution due to incidence of a slender elliptic half-cone. *J. R. Ae. Soc.* Vol. 59, p. 694. 1955.
16	E. W. E. Rogers, C. J. Berry and R. F. Cash	Tests at high subsonic speeds on a 10 per cent thick pressure-plotting aerofoil of RAE 104 section. R. & M. 2863. April, 1951.
17	E. S. Love and C. E. Grigsby ..	A new shadowgraph technique for the observation of conical flow phenomena in supersonic flow and preliminary results obtained for a triangular wing. N.A.C.A. T.N.2950. 1953.
18	Tomotika and Tamada	Application of the hodograph method to the flow of a compressible fluid past an elliptic cylinder. *Proc. Phys. Math. Soc.* Japan, Vol. 23, p. 958. 1941
19	H. Werlé	Quelques résultats expérimentaux sur les ailes en flèche, aux faibles vitesses, obtenus en tunnel hydrodynamique. *La Recherche Aeronautique*, p. 15. September, 1954.
20	R. Legendre	Ecoulement au voisinage de la pointe avont d'une aile à forte flèche aux incidences moyennes. *La Recherche Aeronautique.* November, 1952 and January, 1953.
21	P. T. Fink	Some low-speed aerodynamic properties of cones. Experiments done in the Imperial College Aeronautical Laboratory. A.R.C. 17,632. 28th February, 1955.
See	P. T. Fink and also J. Taylor ..	Some low-speed experiments with 20-deg delta wings. A.R.C. 17,854. September, 1955.
22	T. Örnberg	A note on the flow around delta wings. KTH Aero. T.N.38. 1954.

REFERENCES—*conitnued*

No.	*Author*	*Title, etc.*
23	C. Brown and W. Michael ..	Effect of leading-edge separation on the lift of a delta wing. *J. Ae. Sci.* Vol. 21, p. 690. 1954.
24	Mac. C. Adams	Leading-edge separation from delta wings at supersonic speeds. *J. Ae. Sci.* Vol. 20, p. 430. 1953.
25	H. J. Allan and E. Perkins ..	A study of the effects of viscosity on flow over slender inclined bodies of revolution. N.A.C.A. Report 1048. 1951.
26	F. Moore	Three-dimensional laminar boundary-layer flow. *J. Ae. Sci.* Vol. 20, p. 525. 1953.
27	J. B. Scott-Wilson and D. S. Capps	Wind-tunnel observations of boundary layer transition on two swept-back wings at a Mach number of 1·61. R.A.E. T.N.Aero. 2347. A.R.C. 17,627. December, 1954.
28	A. H. Flax and H. R. Lawrence	The aerodynamics of low-aspect-ratio wings and wing-body combinations. *Proc. Joint R. Ae. Soc.* and *I. Ae. Sci. Conference*, p. 363. 1951.
29	N. Delany and N. Sorensen ..	Low-speed drag of cylinders of various shapes. N.A.C.A. T.N.3038. 1953.
30	M. M. Munk	The aerodynamic forces on airship hulls. N.A.C.A. Report 184. 1924.
31	—	*A selection of Graphs for use in calculations of Compressible Airflow.* O.U.P. 1954.
32	D. R. Chapman, W. R. Wimbrow and R. H. Kester	Experimental investigation of base pressure on blunt trailing-edge wings at supersonic velocities. N.A.C.A. T.N.2611. 1952.
33	G. E. Gadd, D. W. Holder and J. D. Regan	Base pressures in supersonic flow. C.P.271. March, 1955.
34	D. R. Chapman	An analysis of base pressure at supersonic velocities and comparison with experiment. N.A.C.A. Report 1051. 1951.
35	E. S. Love..	Investigations at supersonic speeds of 22 triangular wings representing two airfoil sections for each of 11 apex angles. N.A.C.A. R.M. L9D07. (NACA/TIB/2135). 1949. Superseded by Report 1238. 1955. A.R.C. 13,759. 1949.
36	C. Adams and W. Sears	Slender-body theory—review and extension. *J. Ae. Sci.* Vol. 20. No. 2, p. 85. 1953.
37	R. W. May and J. G. Hawes ..	Low-speed pressure distribution and flow investigations for a large pitch and yaw range of 3 low-aspect ratio pointed wings having leading-edges swept back 60-deg and biconvex sections. N.A.C.A. R.M. L9J07. 1949.
38	D. Küchemann	A non-linear lifting-surface theory for wings of small aspect ratio with edge separations. R.A.E. Report Aero. 2540. A.R.C. 17,769. April, 1955.
39	H. H. Pearcey and M. E. Faber	Detailed observations made at high incidences and at high subsonic Mach numbers on Goldstein 1442/1547 aerofoil. R. & M. 2849. November, 1950.
40	J. D. Main-Smith..	Chemical solids as diffusible coating films for visual indication of boundary-layer transition in air and water. R. & M. 2755. February, 1950.
41	J. B. Broderick	Supersonic flow round pointed bodies of revolution. *Quart. J. Math. App. Mech.* Vol. 2, p. 98. 1949.

TABLE 2

Lift, Drag, and Centre-of-Pressure Positions for Elliptic Cones

(*a*) Cone C1 ($\varepsilon = 60$ deg, $\tau = 0{\cdot}05$): Balance Readings

α (deg)	C_{Dp}	α (deg)	C_L	Centre-of-pressure position, rear of 2/3 centre-line chord position (f)
0	0·0042	0	0	—
2·2	0·0082	1·4	0·075	0·0080
4·6	0·0206	2·8	0·146	0·0072
7·1	0·0416	4·2	0·216	0·0068
		5·5	0·277	0·0066
		7·0	0·356	0·0058
		8·5	0·422	0·0038

(*b*) Cone C2 ($\varepsilon = 60$ deg, $\tau = 0{\cdot}10$): Pressure Integrations

α (deg)	C_L	C_{Dp}	α (deg)	C_L	C_{Dp}
0	0	0·0162	8·1	0·327	—
1·0	0·057	—	9·2	0·456	0·0767
2·0	0·100	0·0178	10·2	0·489	0·0893
3·0	0·147	—	11·2	0·551	0·1103
4·1	0·202	0·2057	12·2	0·595	0·1290
5·1	0·244	0·0310	13·2	0·645	0·1560
6·1	0·298	0·0414	14·3	0·695	0·1786
7·1	0·347	0·0498	15·3	0·730	—

(*c*) Cone C3 ($\varepsilon = 60$ deg, $\tau = 0{\cdot}15$): Balance Readings

α (deg)	C_L	C_{Dp}	f	α (deg)
0	0	0·0305	—	0
1·2	0·060	0·0315	−0·0046	1·1
2·4	0·120	0·0330	+0·0006	2·2
3·6	0·172	0·0360	0·0018	3·3
4·8	0·219	0·0417	0·0006	4·4
6·0	0·290	0·0497	0·0020	5·5
7·2	0·347	0·0596	0·0024	6·6
8·4	0·406	0·0738	0·0034	7·7
9·6	0·466	0·0907	0·0030	8·8
10·8	0·527	0·1127	0·0018	9·9
			+0·0016	11·0

(*d*) Cone C4 ($\varepsilon = 60$ deg, $\tau = 0{\cdot}20$):

(i) *Balance Readings*

α (deg)	C_L	f	α (deg)	C_{Dp}
0	0			
1·1	0·054	—	0	0·0575
2·2	0·103	−0·0048	2·4	0·0599
3·3	0·161	−0·0030	4·8	0·0701
4·4	0·209	−0·0018	7·2	0·0865
5·5	0·251	−0·0006	9·6	0·1136
6·6	0·305	−0·0020	10·8	0·1335
7·7	0·362	−0·0014		
8·8	0·410	+0·0008		
9·9	0·465	0·0006		
11·0	0·520	0·0010		
12·1	0·577	0·0004		
13·2	0·618	0		
		+0·0018		

(ii) *Pressure Integrations*

α (deg)	C_L	C_{Dp}	α (deg)	C_L	C_{Dp}
0	0	0·0560	8·1	0·387	0·0946
1·0	0·056	—	9·2	0·428	0·1075
2·0	0·098	0·0581	10·2	0·488	0·1230
3·0	0·152	0·0620	11·2	0·534	0·1393
4·1	0·194	0·0659	12·2	0·590	0·1586
5·1	0·241	0·0704	13·2	0·630	0·1763
6·1	0·293	0·0780	14·3	0·675	0·2009
7·1	0·330	0·0834			

(*e*) Cone C5 ($\varepsilon = 30$ deg, $\tau = 0{\cdot}10$): Balance Readings

α (deg)	C_L	f	α (deg)	C_{Dp}
0	0	—	0	0·0086
1·0	0·028	−0·0022	2·1	0·0108
2·0	0·050	—	4·2	0·0161
3·0	0·084	+0·0006	6·3	0·0261
4·1	0·109	0·0012	8·4	0·0423
5·1	0·141	+0·0004	10·5	0·0681
6·1	0·166	−0·0006	12·6	0·0972
7·2	0·198	−0·0020	14·8	0·1345
8·2	0·233	0		
9·2	0·270	+0·0010		
10·3	0·310	0·0028		
11·3	0·350	0·0040		
12·3	0·381	0·0012		
13·4	0·419	+0·0036		
14·4	0·444	−0·0020		

(*f*) Cone C6 ($\varepsilon = 90$ deg, $\tau = 0{\cdot}10$): Balance Readings

α (deg)	C_L	f	α (deg)	C_{Dp}
0	0	—	0	0·0238
1·3	0·091	−0·0008	1·3	0·0242
2·6	0·173	−0·0028	2·6	0·0277
3·8	0·255	−0·0042	3·8	0·0335
5·1	0·334	−0·0044	5·1	0·0424
6·3	0·414	−0·0052	6·3	0·0524

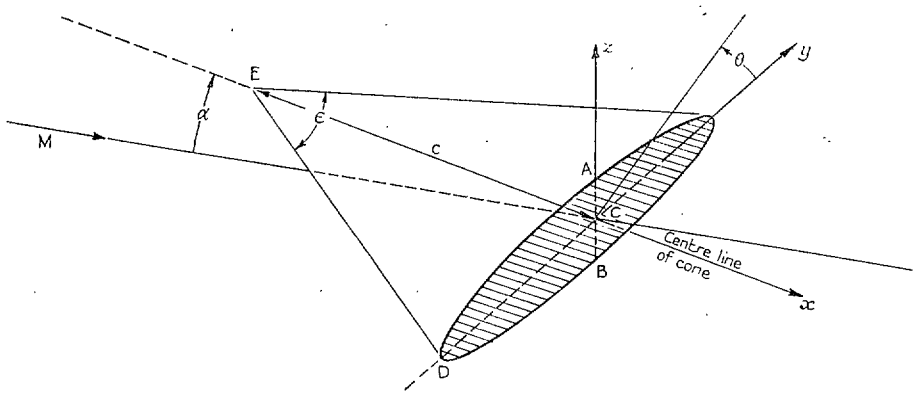

FIG. 1. Elliptic cone model.

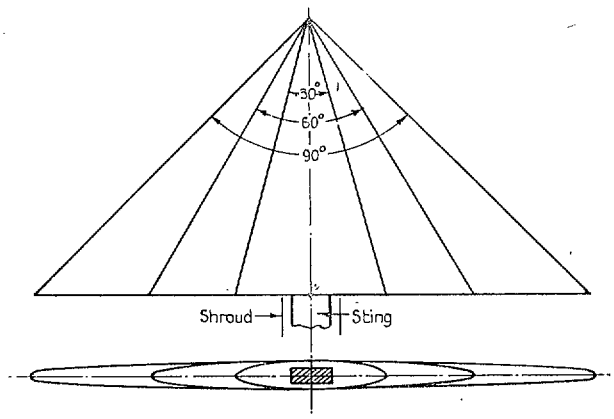

(a) Elliptic cone family with $\tau = 0{\cdot}1$.

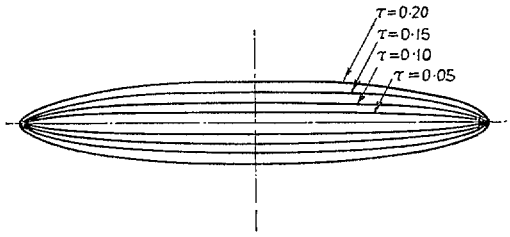

(b) Elliptic cross-sections of 60° vertex angle family

FIGS. 2a and 2b.
Plan-forms and cross-sections of elliptic cones.

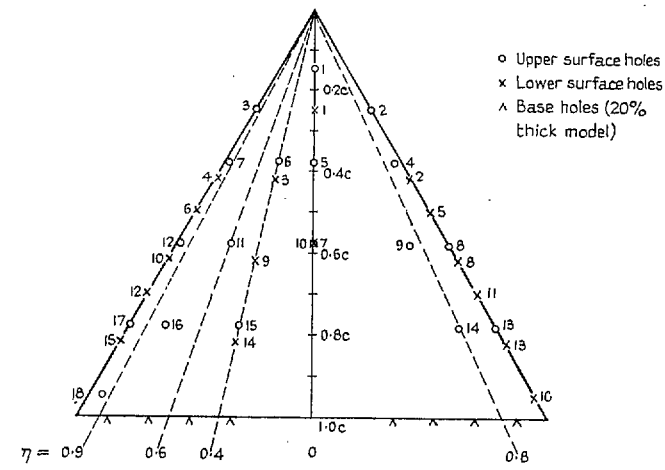

(a) Pressure hole positions on both pressure plotting models ($\epsilon = 60°$)

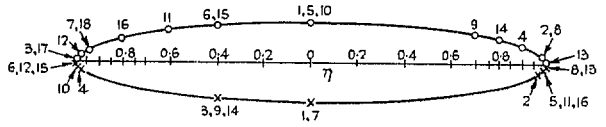

(b) Disposition of pressure holes in terms of η

FIGS. 3a and 3b. Pressure-plotting models.

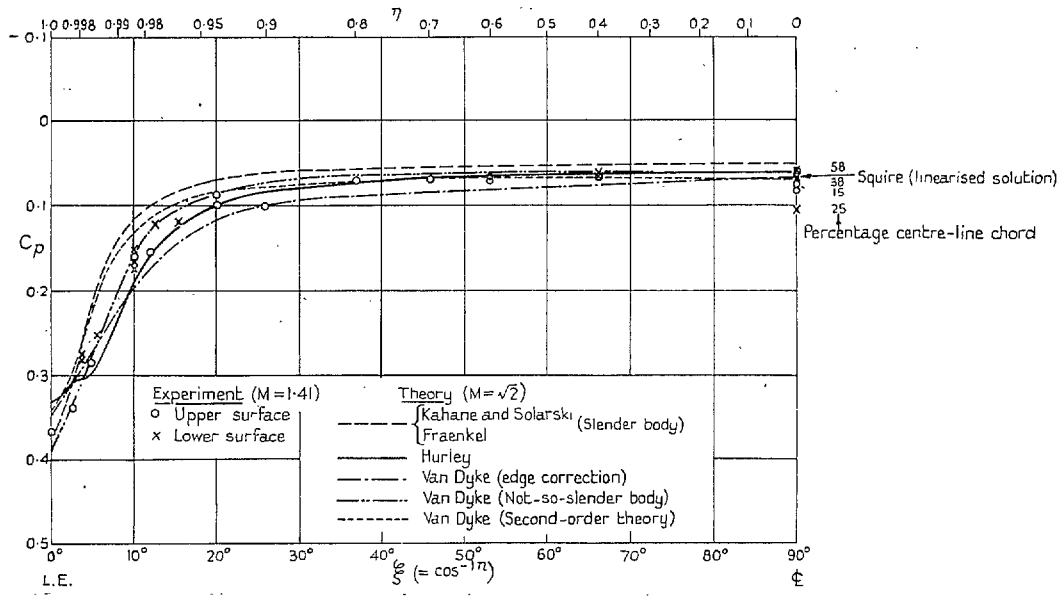

FIG. 4a. Comparison of theoretical and experimental spanwise pressures on cone with $\varepsilon = 60$ deg, $\tau = 0{\cdot}1$, $\alpha = 0$ deg.

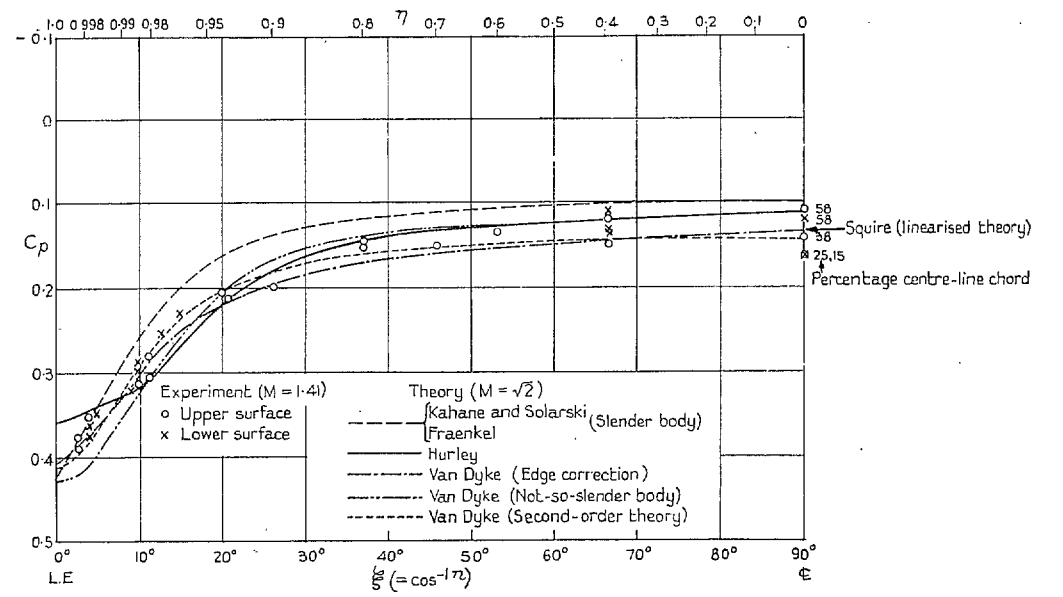

FIG. 4b. Comparison of theoretical and experimental spanwise pressures on cone with $\varepsilon = 60$ deg, $\tau = 0{\cdot}2$, $\alpha = 0$ deg.

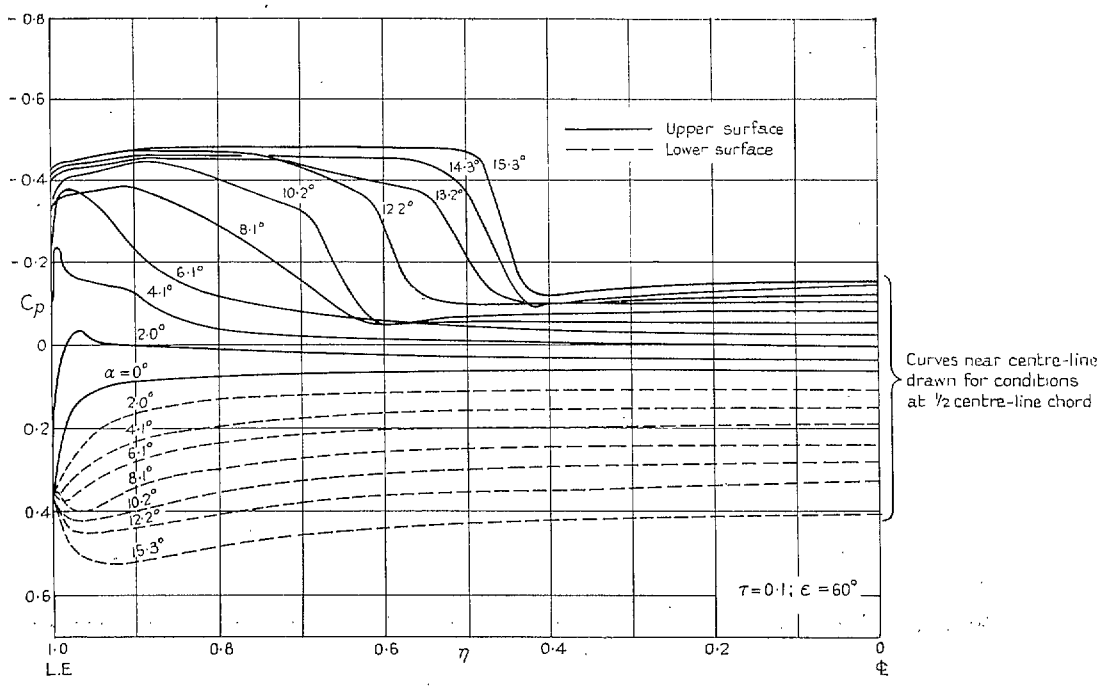

FIG. 5a. Experimental pressure distributions on model C2.

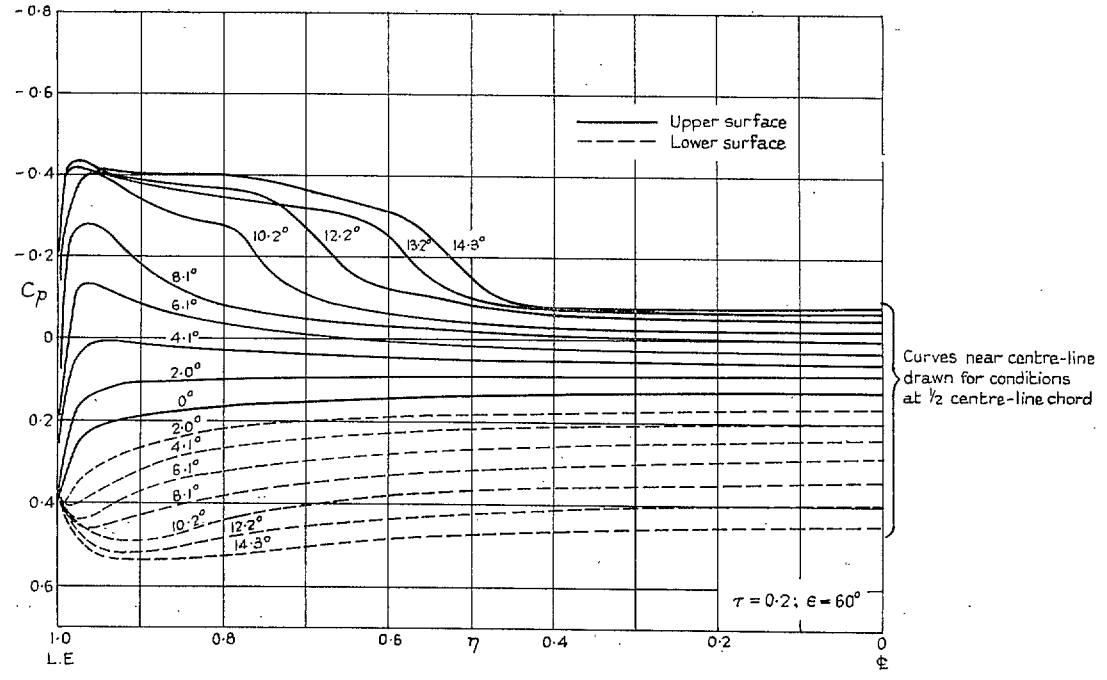

FIG. 5b. Experimental pressure distributions on model C4.

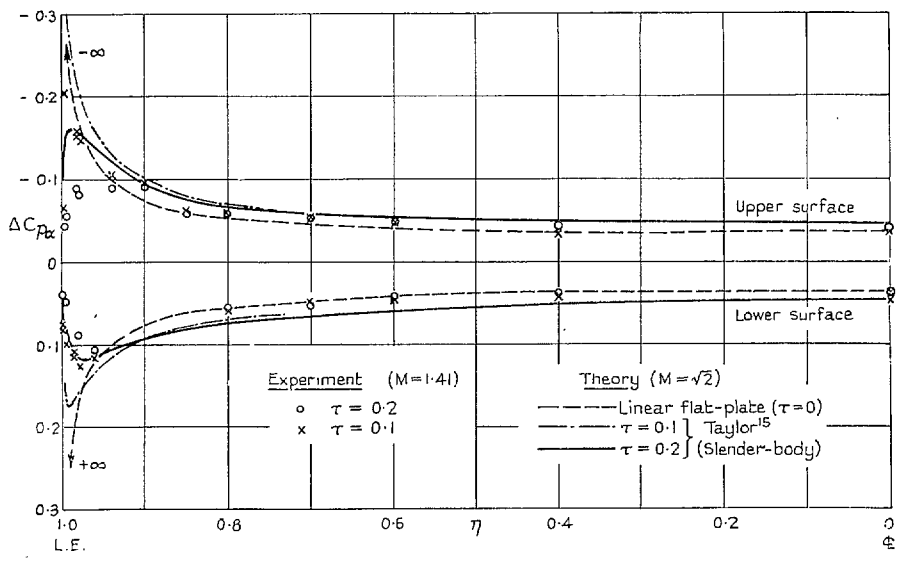

FIG. 6a. Pressure increment due to incidence ($\alpha = 2{\cdot}0$ deg).

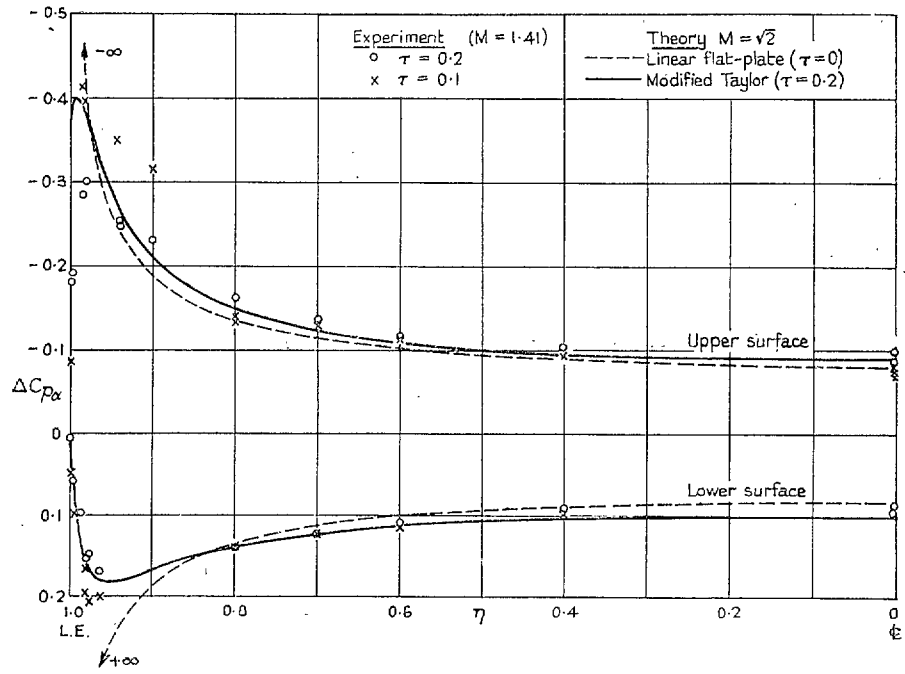

FIG. 6b. Pressure increment due to incidence ($\alpha = 5{\cdot}1$ deg).

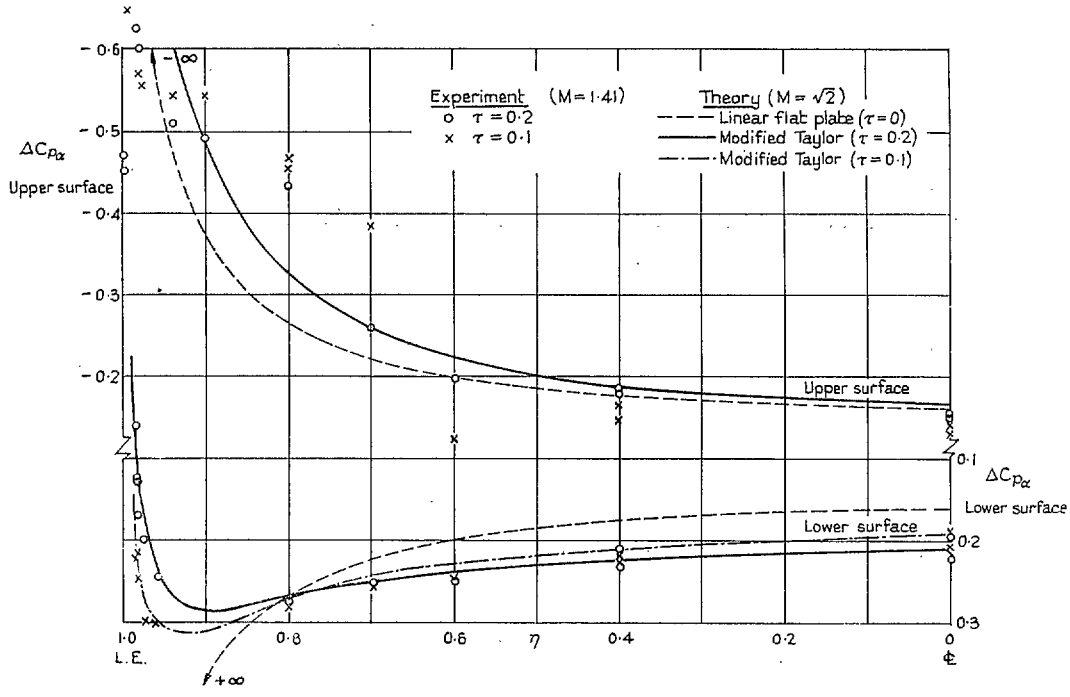

FIG. 6c. Pressure increment due to incidence ($\alpha = 10{\cdot}2$ deg).

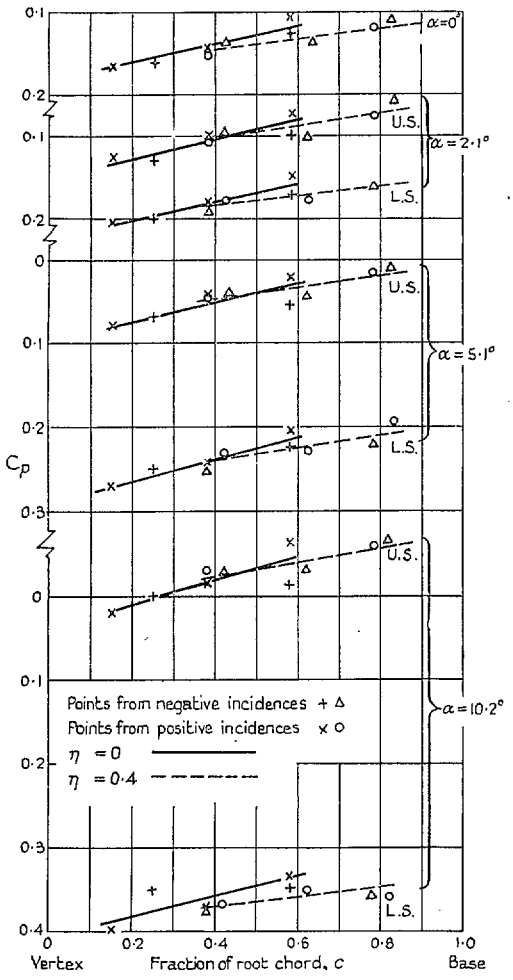

FIG. 7a. Chordwise pressure variations for constant values of η ($\tau = 0{\cdot}1$).

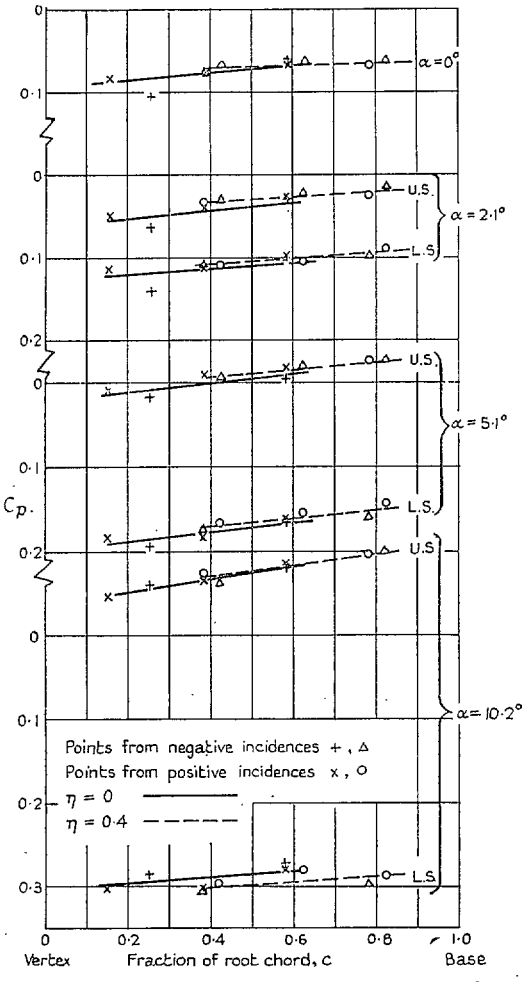

FIG. 7b. Chordwise pressure variations for constant values of η ($\tau = 0{\cdot}2$).

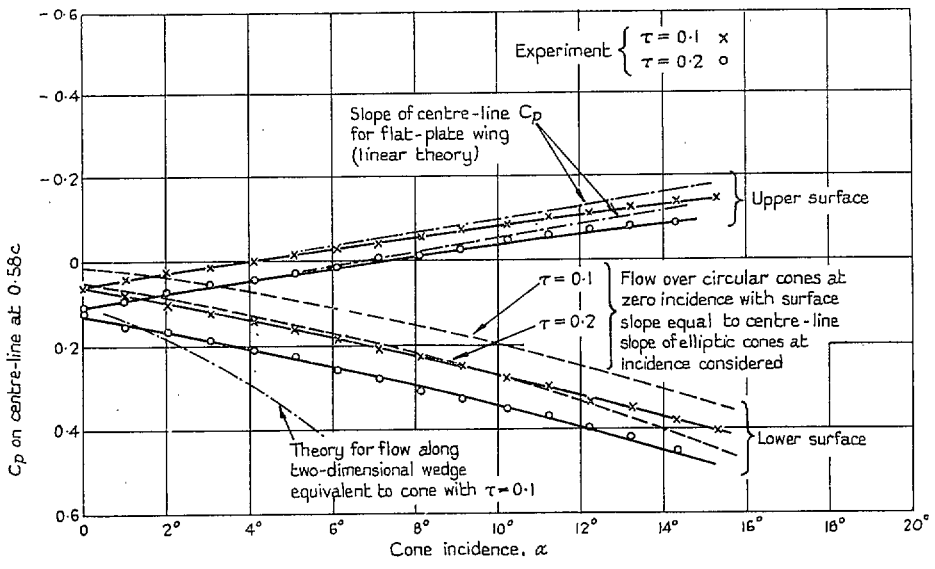

FIG. 8. Variation of C_p on centre-line with incidence.

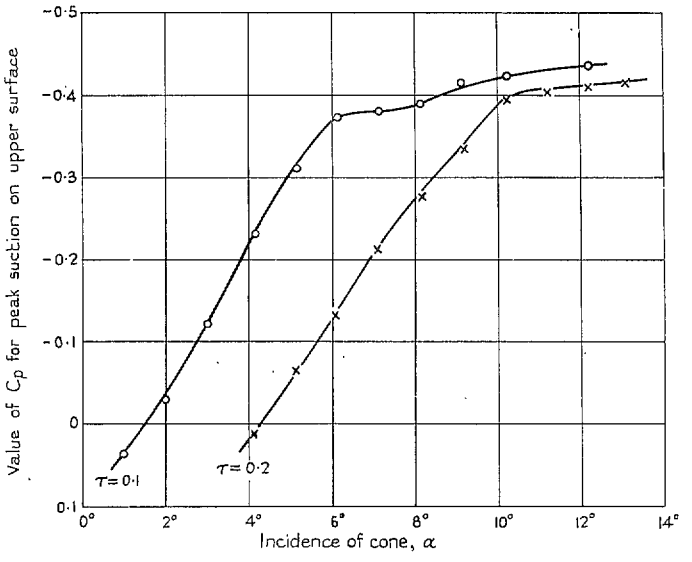

FIG. 9. Peak suction values attained on cones C2 and C4.

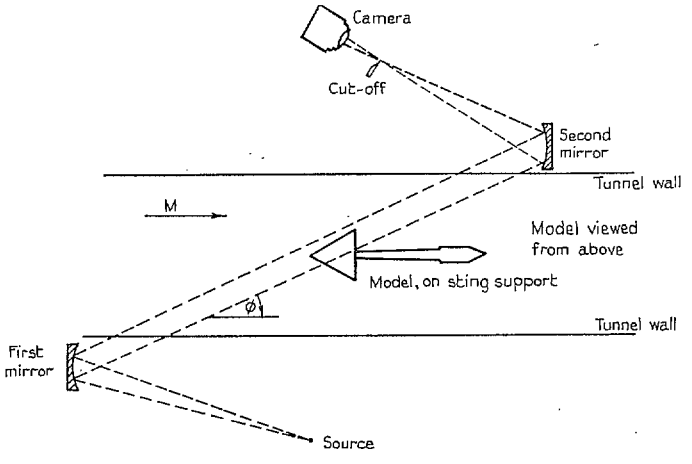

FIG. 10. Diagram of path of light beam for oblique schlieren photographs.

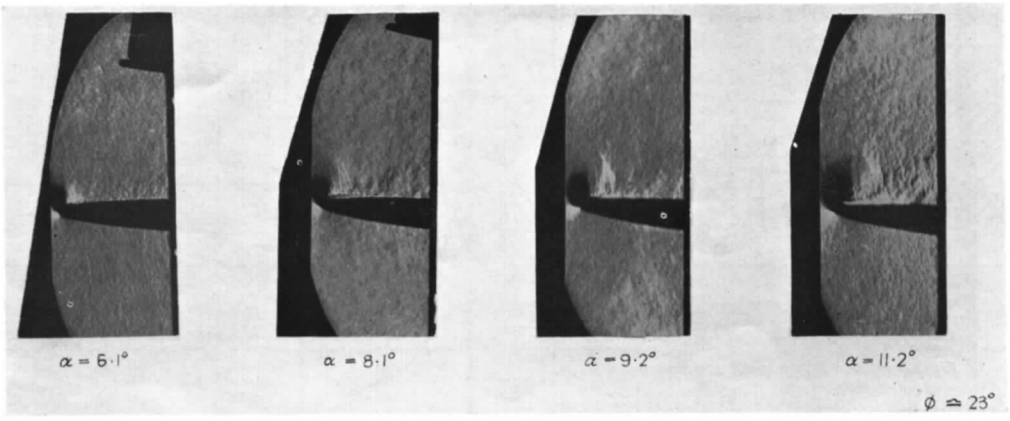

FIG. 11a. Oblique schlieren photographs of surface shock waves on cone C2 ($\varepsilon = 60$ deg, $\tau = 0{\cdot}1$).

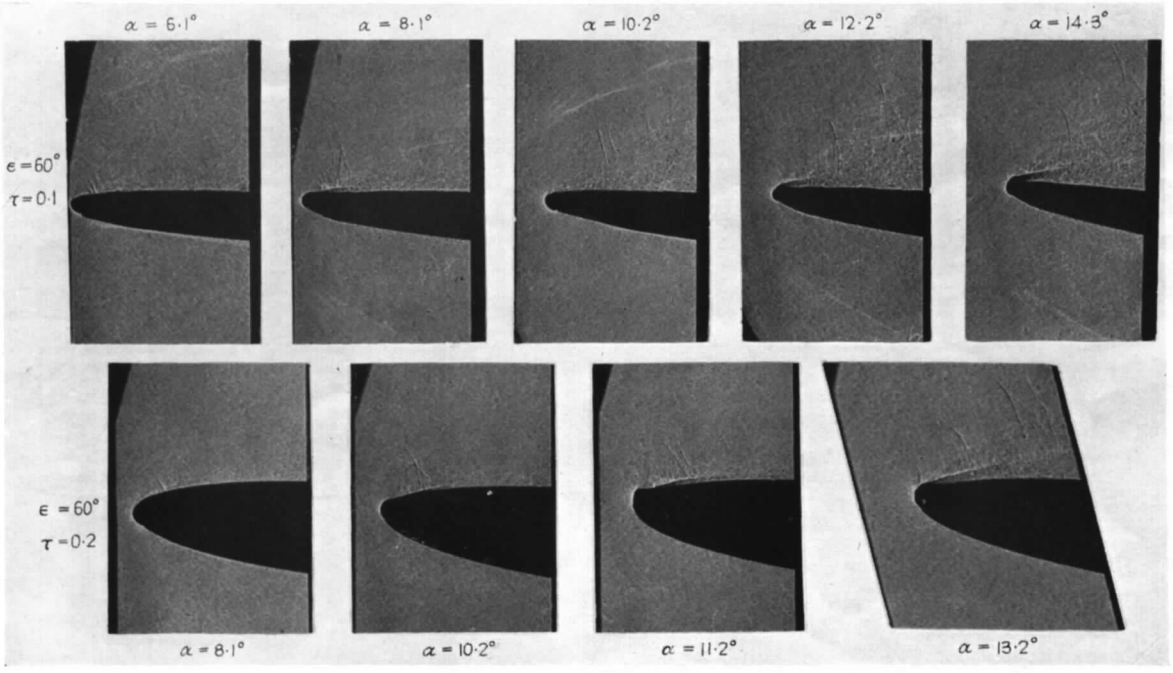

FIG. 11b. Oblique shadow photographs showing flow separation near leading edge ($\phi \simeq 23$ deg).

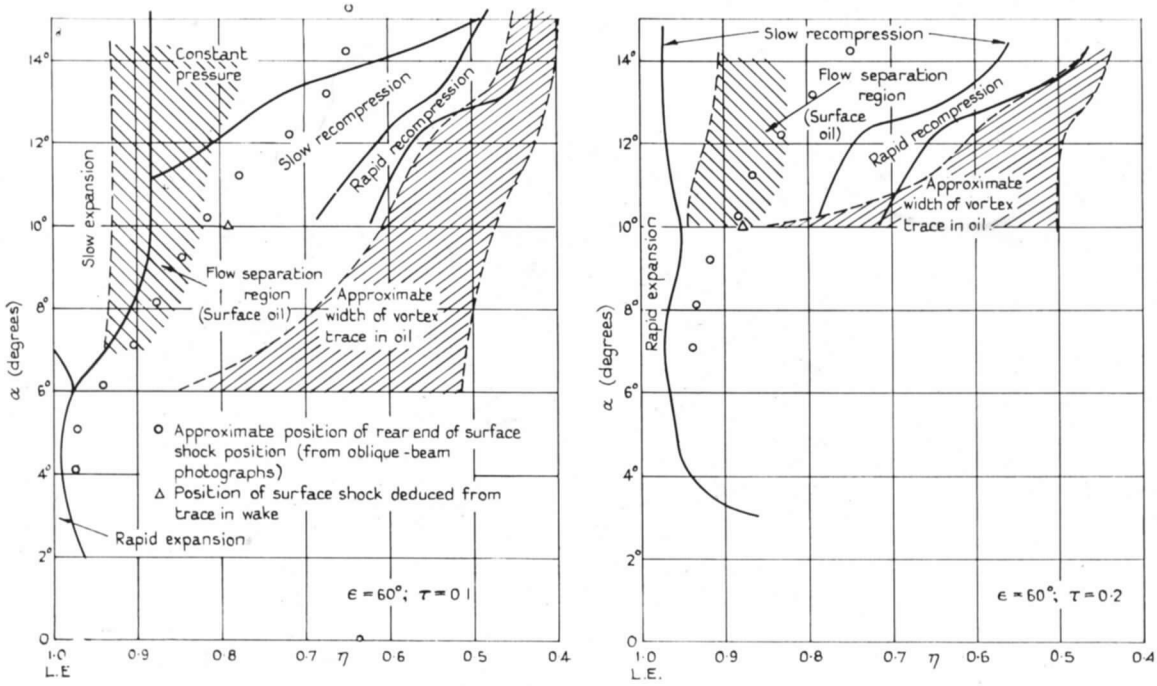

FIG. 12. Relationship between surface-pressure distribution and shock and vortex movement.

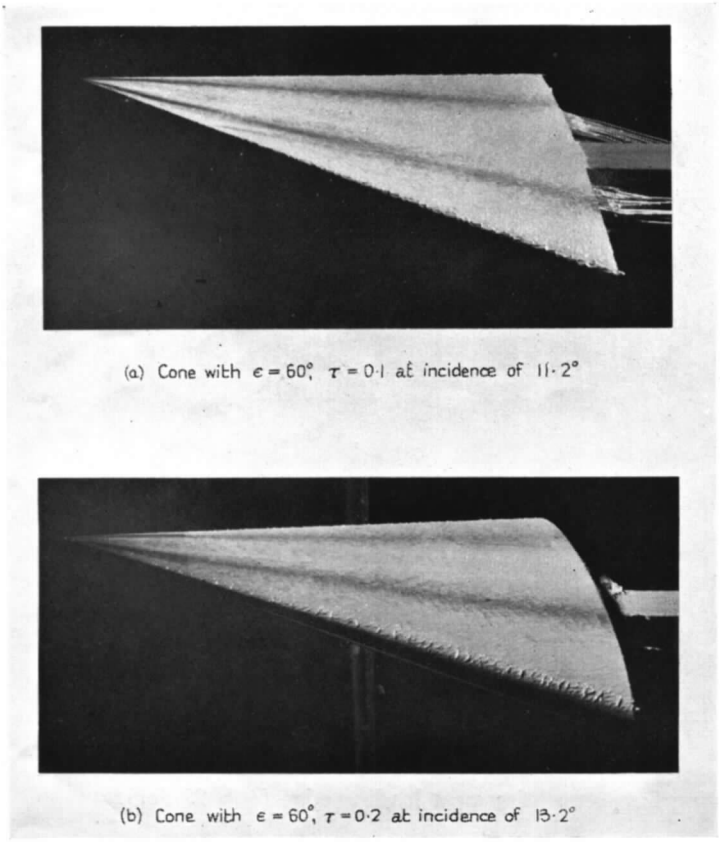

(a) Cone with $\epsilon = 60°$, $\tau = 0{\cdot}1$ at incidence of $11{\cdot}2°$

(b) Cone with $\epsilon = 60°$, $\tau = 0{\cdot}2$ at incidence of $13{\cdot}2°$

FIGS. 13a and 13b. Typical vortex traces. Photographs obtained with tunnel running.

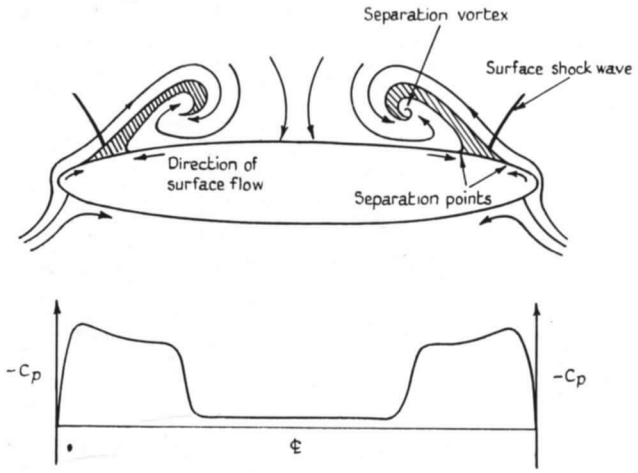

FIG. 14. Diagram of possible cross-flow about elliptic cone.

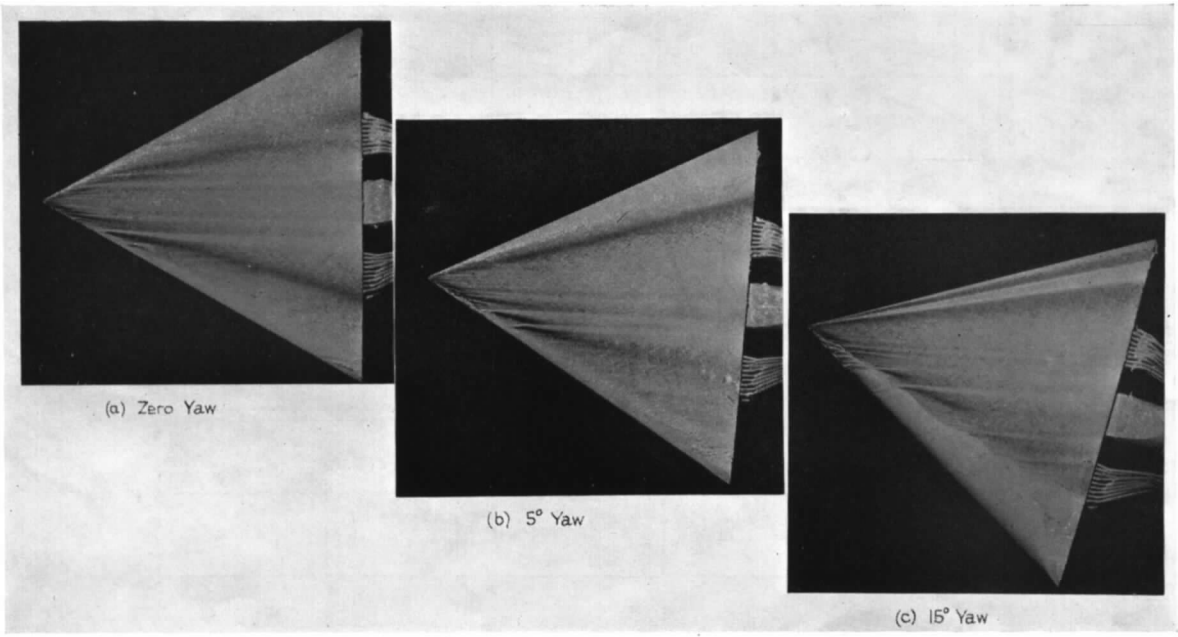

FIGS. 15a to 15c. Effect of yaw on vortex traces at incidence of 10 deg (Cone C2, $\varepsilon = 60$ deg, $\tau = 0{\cdot}1$).

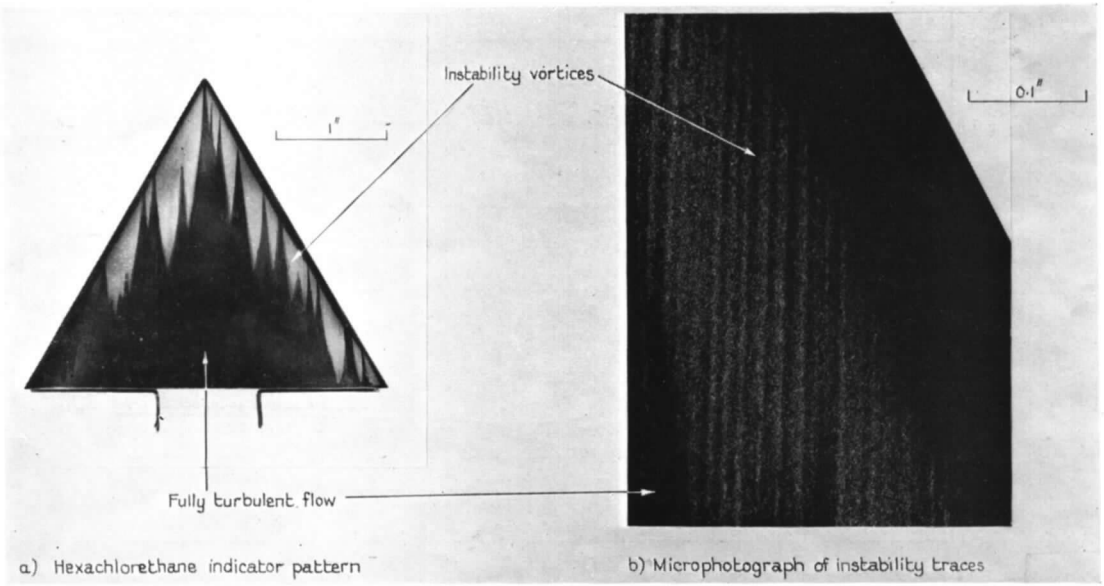

FIGS. 16a and 16b. Three-dimensional boundary-layer instability at $\alpha = 0$ deg on cone C4 ($\varepsilon = 60$ deg, $\tau = 0{\cdot}2$).

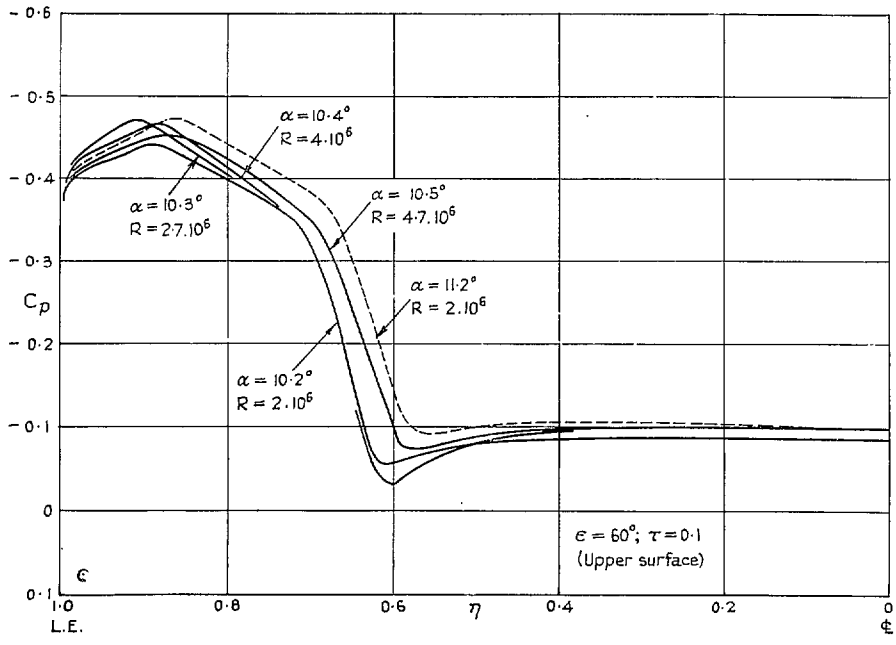

FIG. 17a. Effect of Reynolds number changes on spanwise pressure distribution.

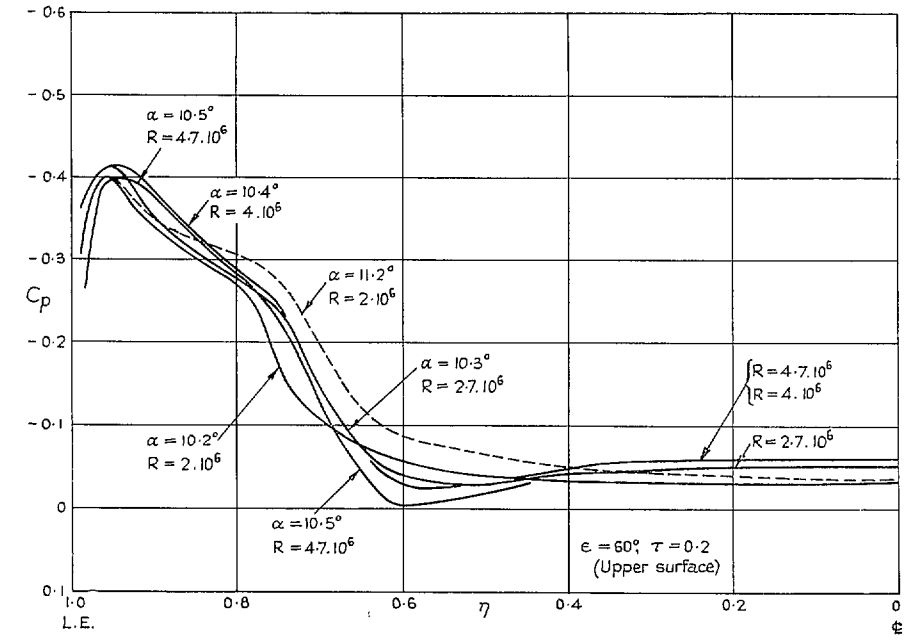

Fig. 17b. Effect of Reynolds number changes on spanwise pressure distribution.

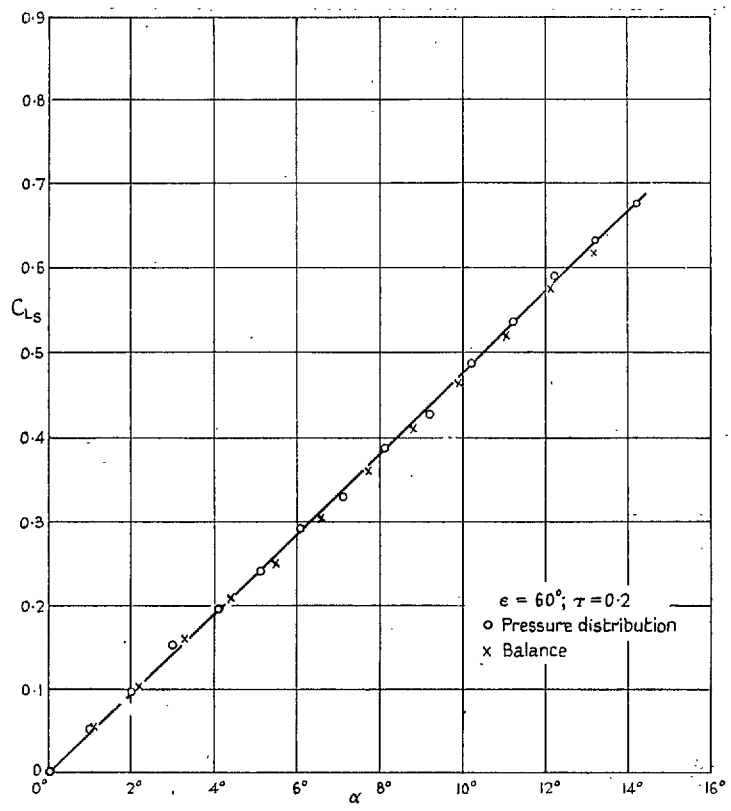

FIG. 18a. Comparison of cone lift curves obtained by two methods.

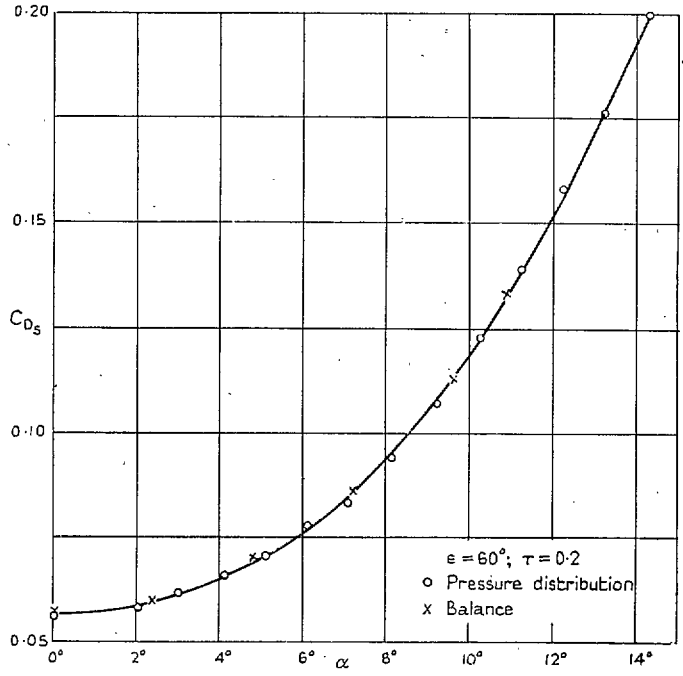

FIG. 18b. Comparison of cone pressure-drag coefficients obtained by two methods.

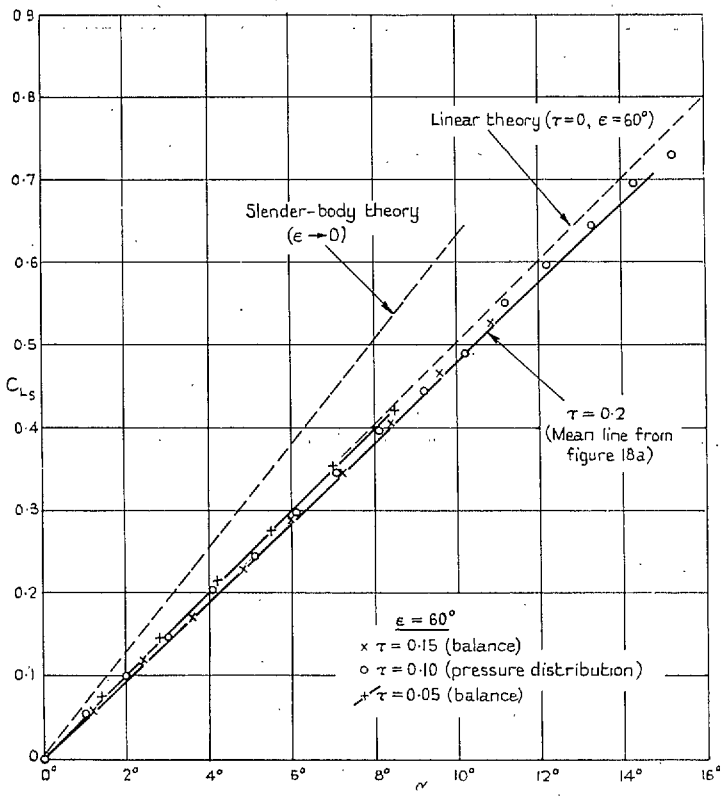

FIG. 19a. Lift curves for 60 deg cone family.

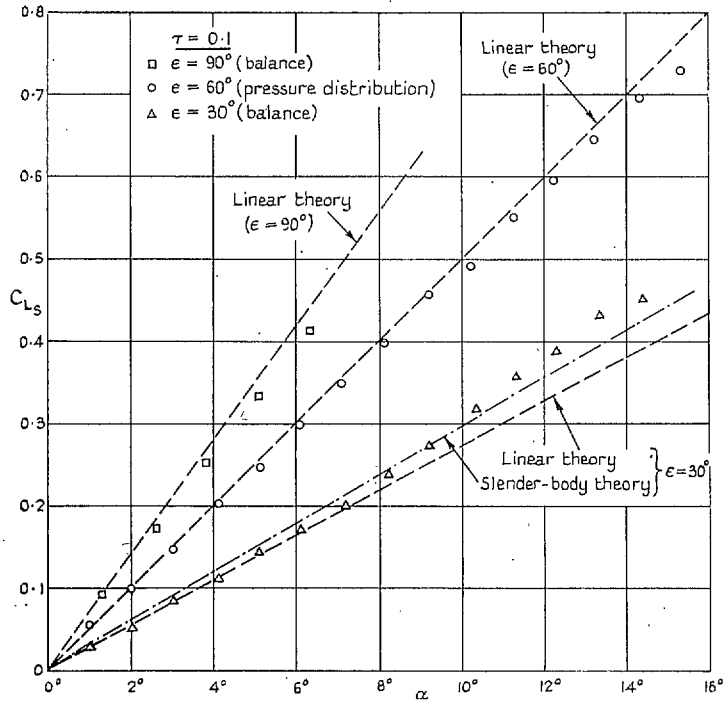

FIG. 19b. Lift curves for cone family with $\tau = 0{\cdot}1$.

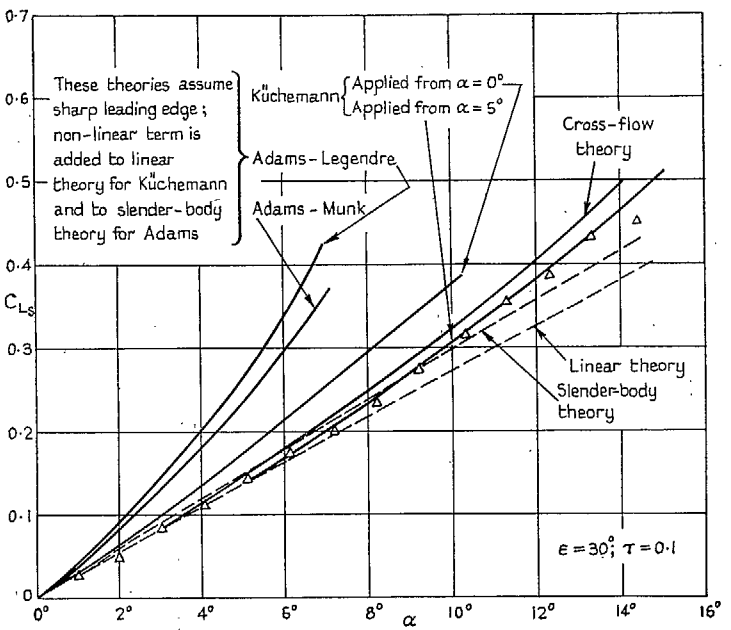

FIG. 19c. Comparison of theory with experiment for cone C5.

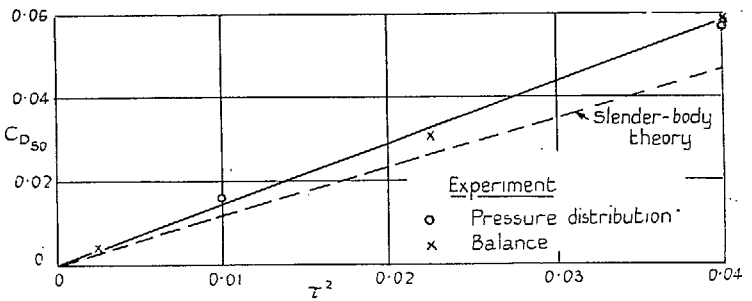

FIG. 20a. Drag coefficient at zero incidence for 60 deg cone family,

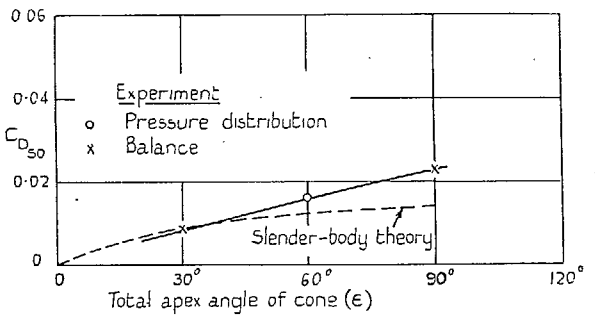

FIG. 20b. Drag coefficient at zero incidence for family with $\tau = 0{\cdot}1$.

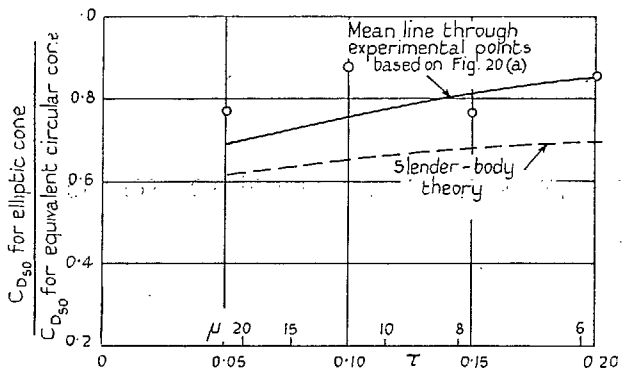

(a) 60° cone family

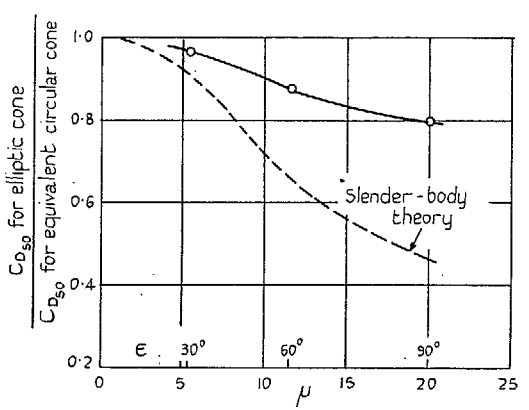

(b) Family with $\tau = 0{\cdot}1$

FIGS. 21a and 21b. Comparison of drag of elliptic cones at zero incidence with that of circular cones having the same base area.

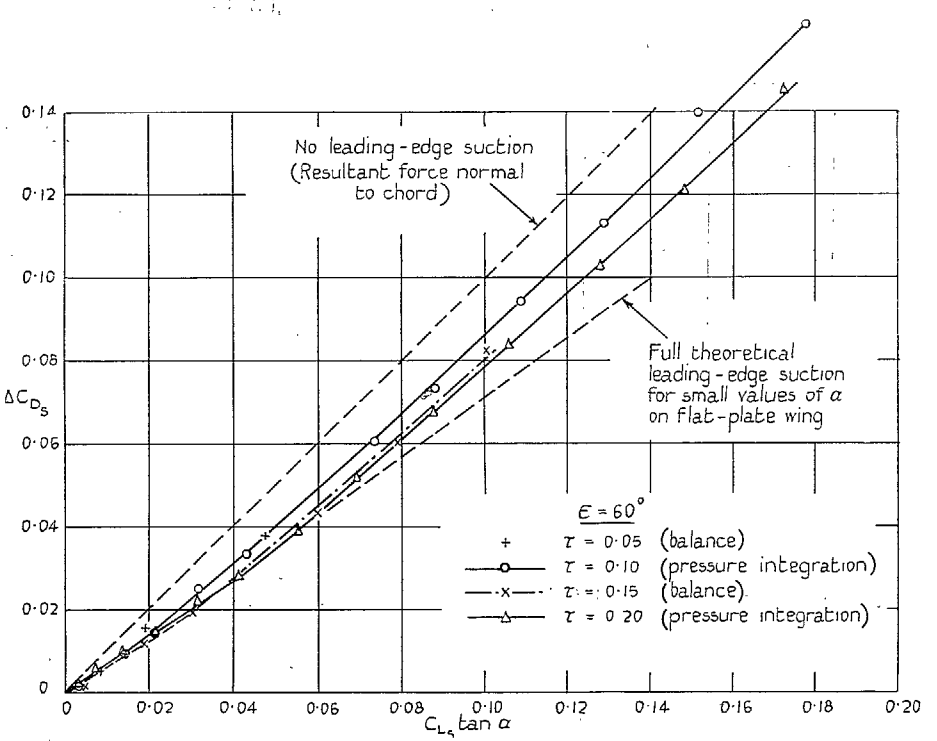

FIG. 22a. Drag-due-to-lift curves for cone family with $\varepsilon = 60$ deg.

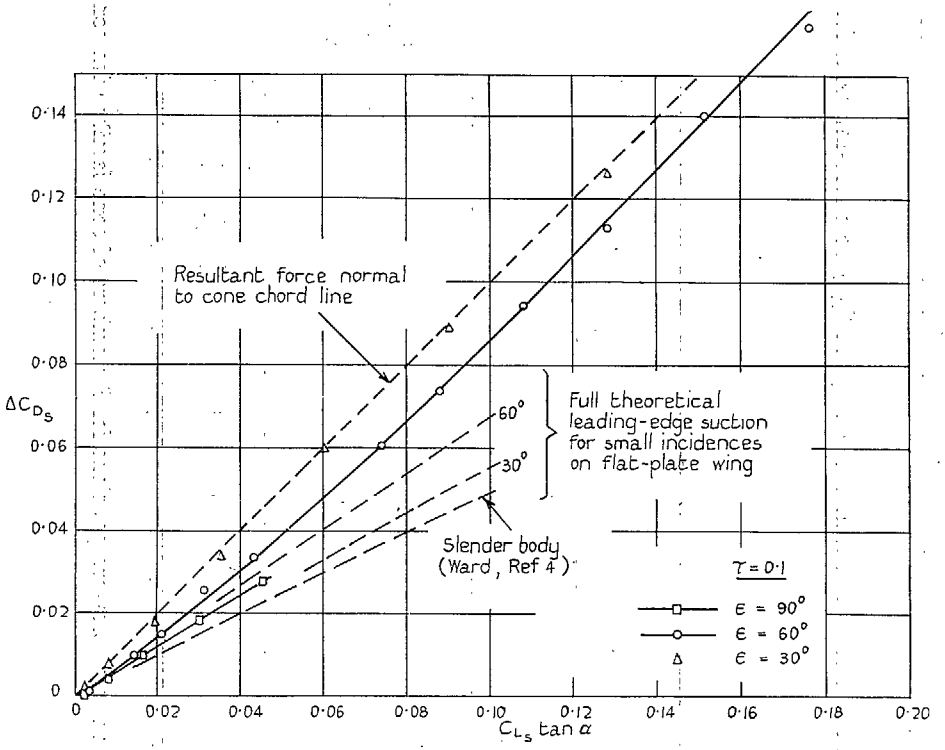

FIG. 22b. Drag-due-to-lift curves for cone family with $\tau = 0{\cdot}1$.

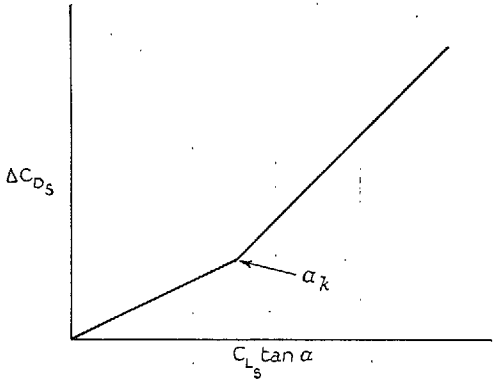

Idealised representation of drag curves of Fig 21

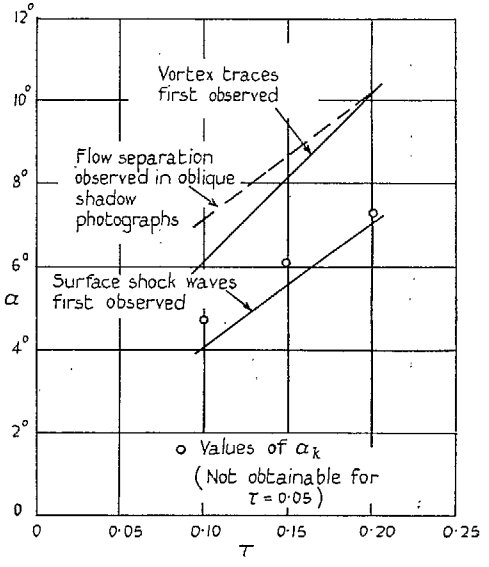

FIG. 23.
Variation of α_k with cone thickness ($\varepsilon = 60$ deg).

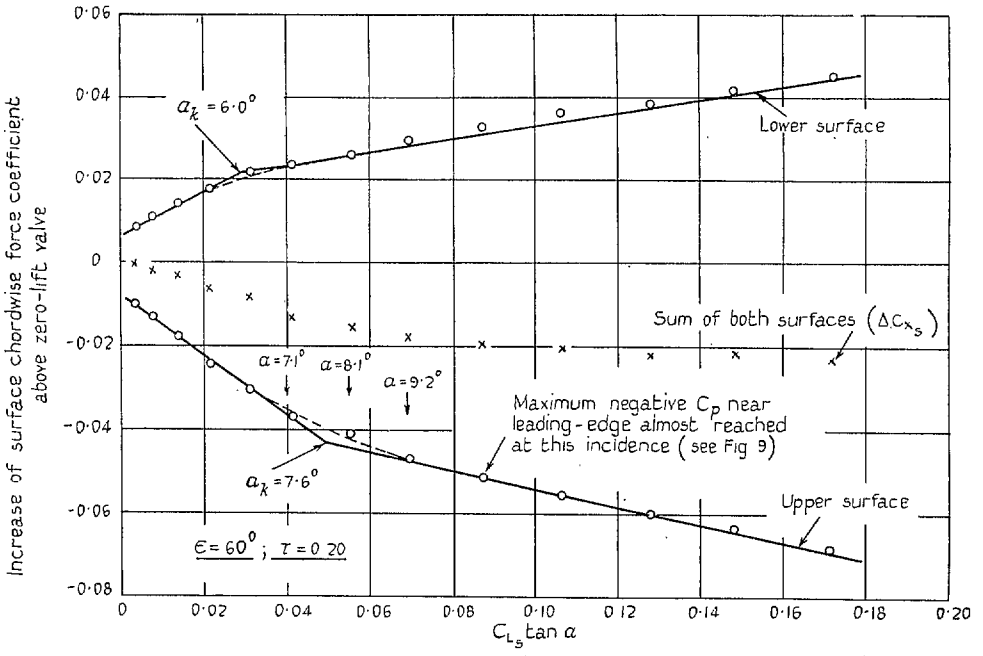

FIG. 24. Idealised two-line representation of change in C_{X_S} from zero-lift value for each surface.

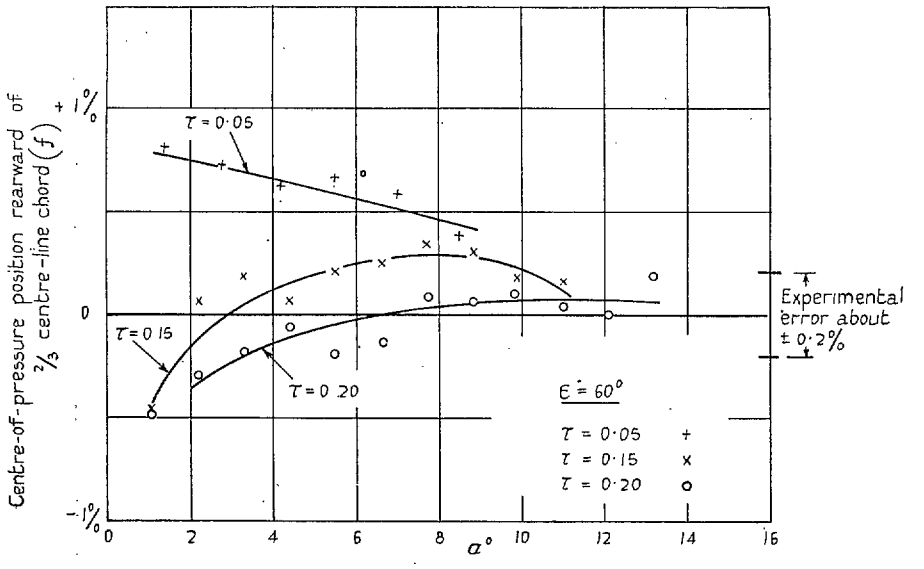

FIG. 25a. FIG. 25a. Centre-of-pressure positions for 3 members of cone family with constant apex angle.

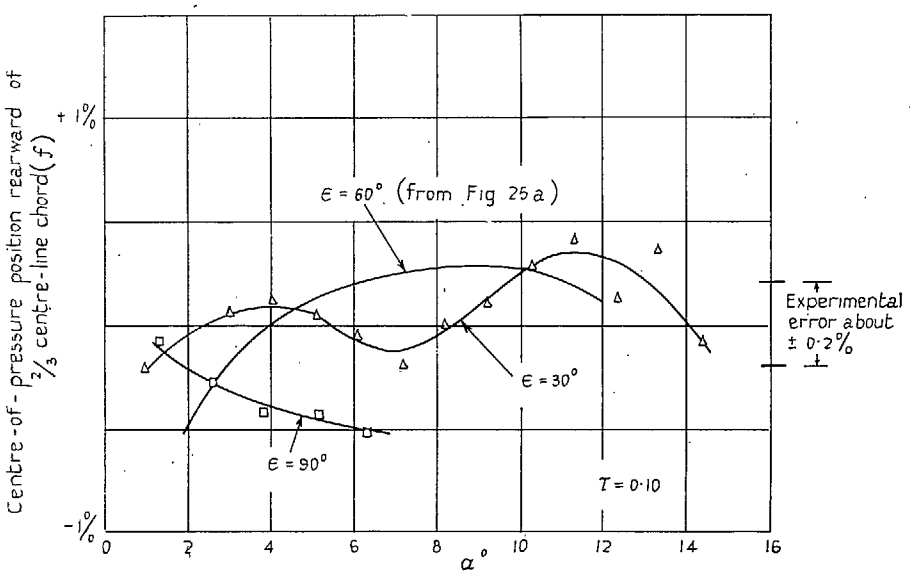

FIG. 25b. Centre-of-pressure positions for cone family with constant thickness.

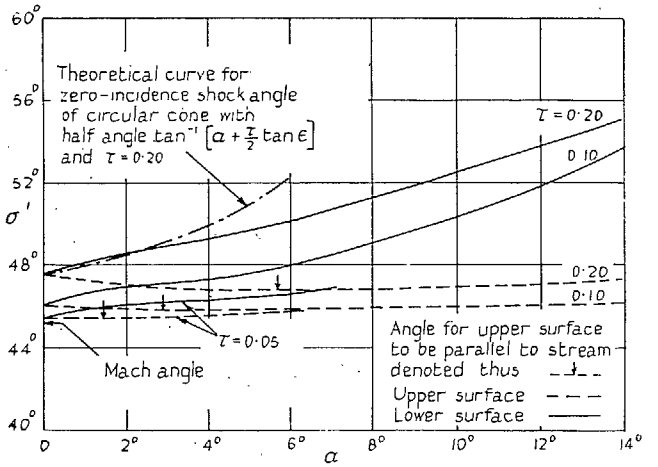

(a) Cone family with $\epsilon = 60°$

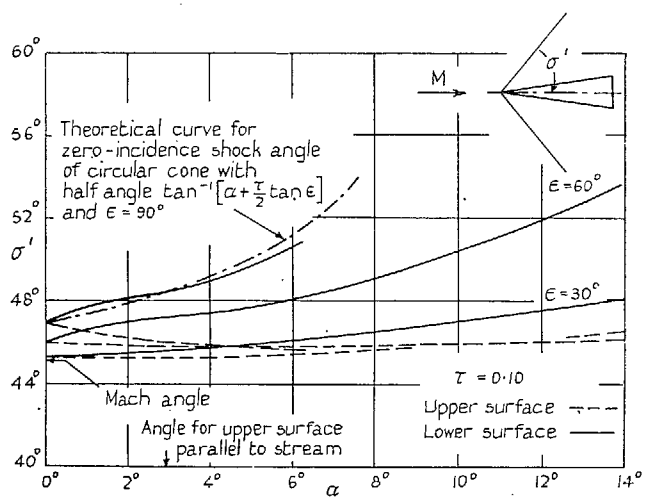

(b) Cone family with $\tau = 0·10$

FIG. 26a and 26b. Shock angles in plane of minor axes for two cone families.

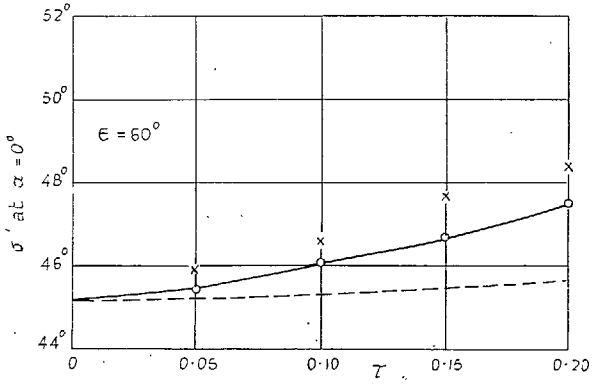

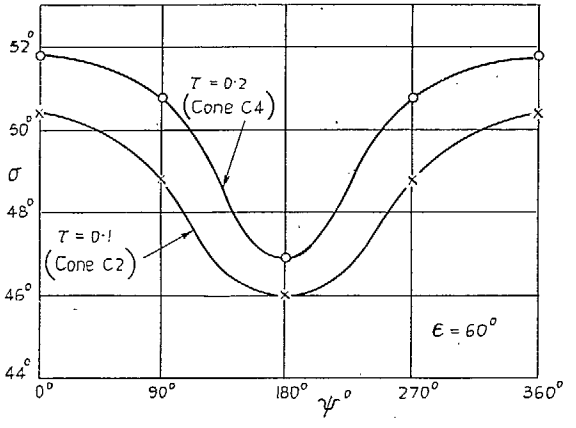

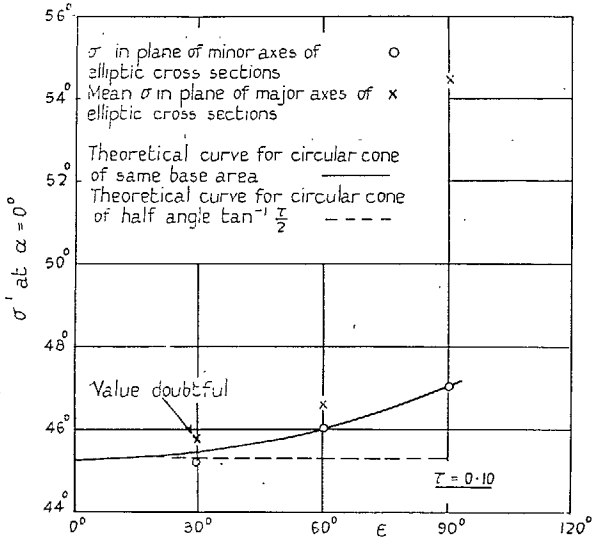

FIG. 27a. Shock angles at zero incidence.

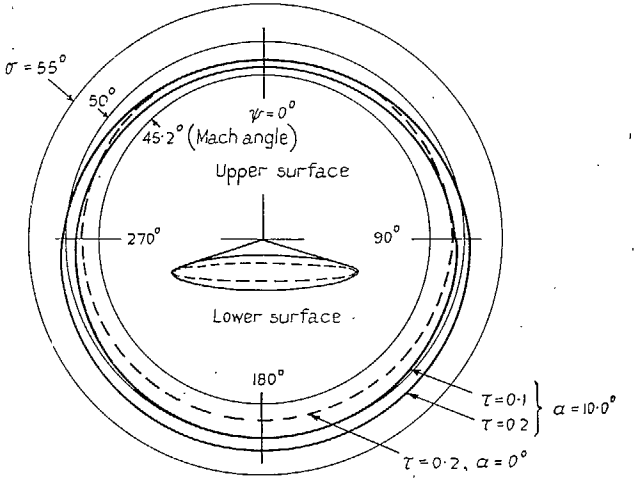

FIG. 27b. Vertex-shock shape for cones C2 and C4 at $\alpha = 10{\cdot}0$ deg.

(40908) Wt. 52 K7 8/57 F.M. & S.

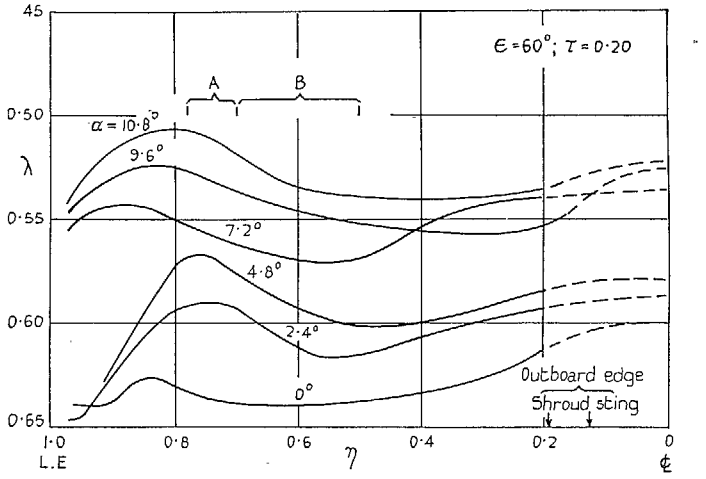

FIG. 28a. Spanwise variation of base pressure for cone C4.

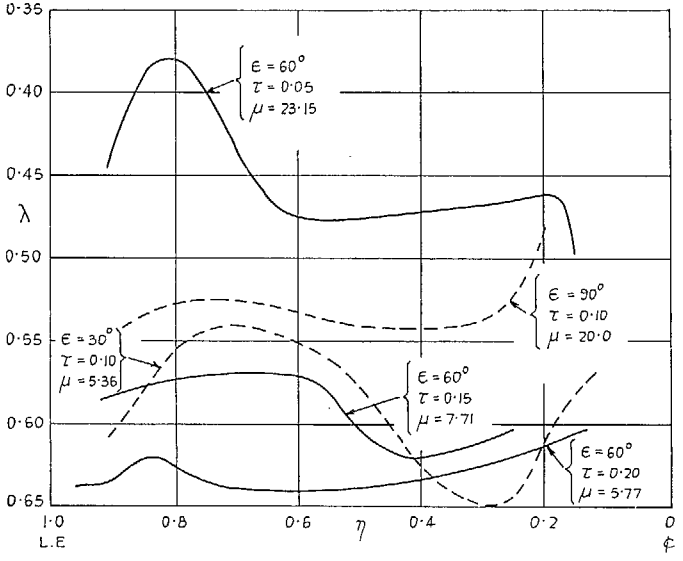

FIG. 28b. Spanwise variation of base pressure at zero incidence.

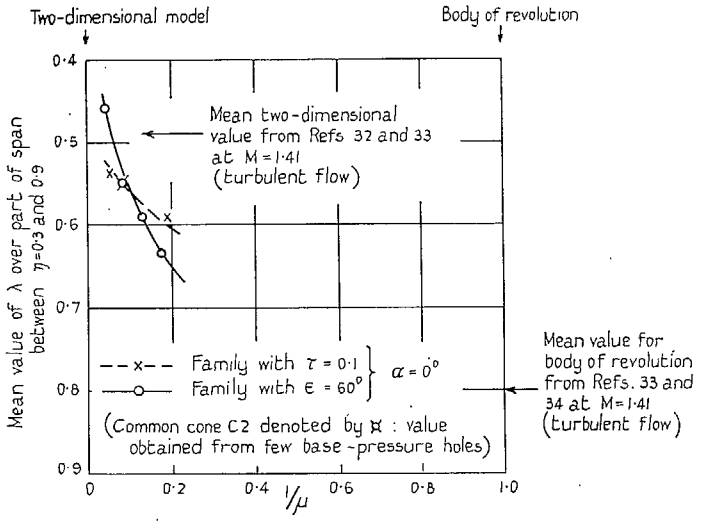

FIG. 28c. Variation of mean base pressure with ratio of base ellipse axes.

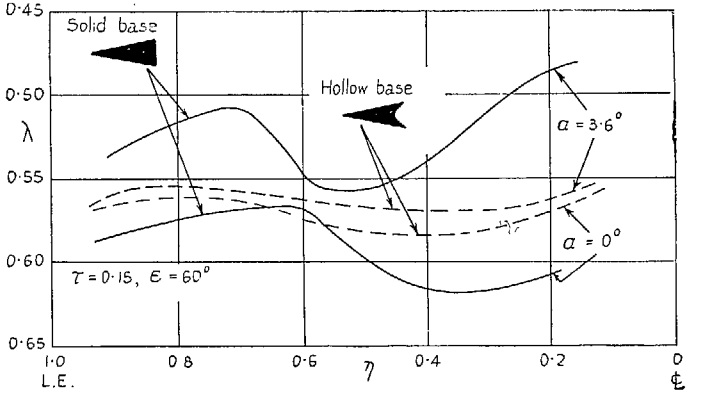

FIG. 28d. Effect of hollowing base of cone C3.

PRINTED IN GREAT BRITAIN

Publication of the Aeronautical Research Council

ANNUAL TECHNICAL REPORTS OF THE AERONAUTICAL RESEARCH COUNCIL (BOUND VOLUMES)

1939 Vol. I. Aerodynamics General, Performance, Airscrews, Engines. 50*s.* (51*s.* 9*d.*).
Vol. II. Stability and Control, Flutter and Vibration, Instruments, Structures, Seaplanes, etc. 63*s.* (64*s.* 9*d.*)

1940 Aero and Hydrodynamics, Aerofoils, Airscrews, Engines, Flutter, Icing, Stability and Control Structures, and a miscellaneous section. 50*s.* (51*s.* 9*d.*)

1941 Aero and Hydrodynamics, Aerofoils, Airscrews, Engines, Flutter, Stability and Control Structures. 63*s.* (64*s.* 9*d.*)

1942 Vol. I. Aero and Hydrodynamics, Aerofoils, Airscrews, Engines. 75*s.* (76*s.* 9*d.*)
Vol. II. Noise, Parachutes, Stability and Control, Structures, Vibration, Wind Tunnels. 47*s.* 6*d.* (49*s.* 3*d.*)

1943 Vol. I. Aerodynamics, Aerofoils, Airscrews. 80*s.* (81*s.* 9*d.*)
Vol. II. Engines, Flutter, Materials, Parachutes, Performance, Stability and Control, Structures. 90*s.* (92*s.* 6*d.*)

1944 Vol. I. Aero and Hydrodynamics, Aerofoils, Aircraft, Airscrews, Controls. 84*s.* (86*s.* 3*d.*)
Vol. II. Flutter and Vibration, Materials, Miscellaneous, Navigation, Parachutes, Performance, Plates and Panels, Stability, Structures, Test Equipment, Wind Tunnels. 84*s.* (86*s.* 3*d.*)

1945 Vol. I. Aero and Hydrodynamics, Aerofoils. 130*s.* (132*s.* 6*d.*)
Vol. II. Aircraft, Airscrews, Controls. 130*s.* (132*s.* 6*d.*)
Vol. III. Flutter and Vibration, Instruments, Miscellaneous, Parachutes, Plates and Panels, Propulsion. 130*s.* (132*s.* 3*d.*)
Vol. IV. Stability, Structures, Wind Tunnels, Wind Tunnel Technique. 130*s.* (132*s.* 3*d.*)

Annual Reports of the Aeronautical Research Council—
1937 2*s.* (2*s.* 2*d.*) 1938 1*s.* 6*d.* (1*s.* 8*d.*) 1939–48 3*s.* (3*s.* 3*d.*)

Index to all Reports and Memoranda published in the Annual Technical Reports, and separately—
April, 1950 - - - - R. & M. 2600 2*s.* 6*d.* (2*s.* 8*d.*)

Author Index to all Reports and Memoranda of the Aeronautical Research Council—
1909—January, 1954 R. & M. No. 2570 15*s.* (15*s.* 6*d.*)

Indexes to the Technical Reports of the Aeronautical Research Council—

December 1, 1936—June 30, 1939	R. & M. No. 1850	1*s.* 3*d.* (1*s.* 5*d.*)
July 1, 1939–June 30, 1945	R. & M. No. 1950	1*s.* (1*s.* 2*d.*)
July 1, 1945—June 30, 1946	R. & M. No. 2050	1*s.* (1*s.* 2*d.*)
July 1, 1946—December 31, 1946	R. & M. No. 2150	1*s.* 3*d.* (1*s.* 5*d.*)
January 1, 1947—June 30, 1947	R. & M. No. 2250	1*s.* 3*d.* (1*s.* 5*d.*)

Published Reports and Memoranda of the Aeronautical Research Council—

Between Nos. 2251–2349	R. & M. No. 2350	1*s.* 9*d.* (1*s.* 11*d.*)
Between Nos. 2351–2449	R. & M. No. 2450	2*s.* (2*s.* 2*d.*)
Between Nos. 2451–2549	R. & M. No. 2550	2*s.* 6*d.* (2*s.* 8*d.*)
Between Nos. 2551–2649	R. & M. No. 2650	2*s.* 6*d.* (2*s.* 8*d.*)

Prices in brackets include postage

HER MAJESTY'S STATIONERY OFFICE

York House, Kingsway, London W.C.2; 423 Oxford Street, London W.1 (Post Orders: P.O. Box 569, London S.E.1); 13a Castle Street, Edinburgh 2; 39 King Street, Manchester 2; 2 Edmund Street, Birmingham 3; 109 St. Mary Street, Cardiff; Tower Lane, Bristol, 1; 80 Chichester Street, Belfast, *or through any bookseller.*

S.O. Code No. 23-3042